

NIHAO IX: the role of gas inflows and outflows in driving the contraction and expansion of cold dark matter haloes

Aaron A. Dutton,^{1*} Andrea V. Macciò^{1,2}, Avishai Dekel³, Liang Wang⁴,
Gregory Stinson², Aura Obreja¹, Arianna Di Cintio⁵, Chris Brook⁶,
Tobias Buck², Xi Kang⁴

¹*New York University Abu Dhabi, PO Box 129188 Abu Dhabi, United Arab Emirates*

²*Max-Planck-Institut für Astronomie, Königstuhl 17, D-69117 Heidelberg, Germany*

³*Center for Astrophysics and Planetary Science, Racah Institute of Physics, The Hebrew University, Jerusalem 91904, Israel*

⁴*Purple Mountain Observatory, the Partner Group of MPI für Astronomie, 2 West Beijing Road, Nanjing 210008, China*

⁵*DARK-Carlsberg Fellow, Dark Cosmology Centre, NBI, Juliane Maries Vej 30, DK-2100 Copenhagen, Denmark*

⁶*Ramon y Cajal Fellow, Departamento de Física Teórica, Universidad Autónoma de Madrid, E-28049 Cantoblanco, Madrid, Spain*

Accepted 2016 June 22. Received 2016 June 22; in original form 2016 May 17

ABSTRACT

We use ~ 100 cosmological galaxy formation ‘zoom-in’ simulations using the smoothed particle hydrodynamics code GASOLINE to study the effect of baryonic processes on the mass profiles of cold dark matter haloes. The haloes in our study range from dwarf ($M_{200} \sim 10^{10} M_{\odot}$) to Milky Way ($M_{200} \sim 10^{12} M_{\odot}$) masses. Our simulations exhibit a wide range of halo responses, primarily varying with mass, from expansion to contraction, with up to factor ~ 10 changes in the enclosed dark matter mass at 1 per cent of the virial radius. Confirming previous studies, the halo response is correlated with the integrated efficiency of star formation: $\epsilon_{\text{SF}} \equiv (M_{\text{star}}/M_{200})/(\Omega_b/\Omega_m)$. In addition, we report a new correlation with the compactness of the stellar system: $\epsilon_{\text{R}} \equiv r_{1/2}/R_{200}$. We provide an analytic formula depending on ϵ_{SF} and ϵ_{R} for the response of cold dark matter haloes to baryonic processes. An observationally testable prediction is that, at fixed mass, larger galaxies experience more halo expansion, while the smaller galaxies more halo contraction. This diversity of dark halo response is captured by a toy model consisting of cycles of adiabatic inflow (causing contraction) and impulsive gas outflow (causing expansion). For net outflow, or equal inflow and outflow fractions, f , the overall effect is expansion, with more expansion with larger f . For net inflow, contraction occurs for small f (large radii), while expansion occurs for large f (small radii), recovering the phenomenology seen in our simulations. These regularities in the galaxy formation process provide a step towards a fully predictive model for the structure of cold dark matter haloes.

Key words: – methods: numerical – galaxies: formation – galaxies: haloes – galaxies: structure – cosmology: theory – dark matter

1 INTRODUCTION

Accurately predicting the structural properties of cold dark matter (CDM) haloes is one of the fundamental goals of modern cosmology. A large amount of effort has been spent studying the radial profiles of CDM haloes as a function of halo mass, time and cosmological parameters (e.g., Navarro et al. 1997; Bullock et al. 2001; Macciò et al. 2008; Zhao et al. 2009; Stadel et al. 2009; Navarro et al. 2010; Klypin et al. 2011; Dutton & Macciò

2014; Diemer & Kravtsov 2015; Ludlow et al. 2016). If one ignores the effects of gas dissipation and star formation, these dissipationless simulations make robust predictions that can be used to test, and potentially falsify, the CDM model. One of these predictions is that CDM haloes are roughly scale free with ‘cuspy’ central density profiles, $\rho(r) \propto r^{-\alpha}$, with $\alpha \approx 1.2$.

Observations of massive elliptical galaxies, which have non-negligible uncertainties in subtracting off the stars, favour these cuspy haloes over cores ($\alpha \approx 0$) or contracted haloes (Dutton et al. 2013b; Dutton & Treu 2014; Sonnenfeld et al. 2015). However, observations of dark mat-

* dutton@nyu.edu

ter dominated systems, where subtracting off the baryons is less problematic, have yet to find convincing evidence of these cusps. Rather, they tend to favour shallower inner density slopes $\alpha \lesssim 0.5$ both in low-mass galaxies (e.g., de Blok et al. 2001; Swaters et al. 2003; Goerdt et al. 2006; Walker & Peñarrubia 2011; Oh et al. 2011) and galaxy clusters (e.g., Newman et al. 2013).

These discrepancies are a potentially fatal problem for the CDM paradigm, and has thus motivated studying other flavours of dark matter that have similar behaviour to CDM on large scales, but differ on small scales. Popular examples are warm dark matter (WDM; Pagels & Primack 1982) and self-interacting dark matter (SIDM; Spergel & Steinhardt 2000). One can also consider more exotic models that have a coupling between the dark matter and dark energy (e.g., Macciò et al. 2015).

Since the baryons make up $\Omega_b/\Omega_m \approx 15\%$ (Planck Collaboration et al. 2014) of the mass in the Universe, to first order it might seem reasonable to assume that baryons only have a small effect on the structure of dark matter haloes. However, one needs to consider that baryons and dark matter are not equally mixed. Baryons can dissipate their energy, leading to higher baryon to dark matter ratios in the centres of galaxies. It is not uncommon for the baryons to dominate the mass budget inside galaxy half-light radii (e.g., Fig. 2 of Courteau & Dutton 2015).

Baryonic processes are known that can cause both expansion and contraction of dark matter haloes at small radii. If the accretion of baryons on to the central galaxy is smooth and slow then dark matter haloes should contract adiabatically (Blumenthal et al. 1986; Gnedin et al. 2004). This process can increase the density of dark matter haloes by an order of magnitude. In contrast, other processes can cause the dark matter halo to expand: rapid mass-loss and/or time variability of the potential due to feedback from stars (Navarro et al. 1996; Read & Gilmore 2005; Mashchenko et al. 2006; Pontzen & Governato 2012; Macciò et al. 2012; El-Zant et al. 2016) or Active Galactic Nuclei (AGN; Martizzi et al. 2012, 2013); mergers and stripping of smaller subhaloes that were puffed up by stellar feedback (Dekel et al. 2003); and transfer of energy/angular momentum from baryons to the dark matter via dynamical friction due to minor mergers (El-Zant et al. 2001; Jardel & Sellwood 2009; Johansson et al. 2009; Cole et al. 2011), or galactic bars (Weinberg & Katz 2002; Sellwood 2008).

Supernova feedback that can alter galactic potentials plays other important roles in the formation of galaxies. It is the principle explanation for why galaxy formation is so inefficient in haloes of Milky Way (MW) virial mass ($M_{200} \sim 10^{12} M_\odot$) and below (e.g., Dekel & Silk 1986; Hopkins et al. 2014; Wang et al. 2015). Stellar feedback also ejects low angular momentum material, enabling the formation of exponential disc-dominated galaxies (e.g., Maller & Dekel 2002; Dutton 2009; Brook et al. 2011; Brooks & Christensen 2016). Likewise, AGN feedback is the principle explanation for why galaxy formation is so inefficient in haloes more massive than the MW (e.g., Croton et al. 2006; Somerville et al. 2008).

At the mass scale of the MW early cosmological hydrodynamical simulations almost invariably found that dark matter haloes contract in response to galaxy forma-

tion (e.g., Gustafsson et al. 2006; Romano-Díaz et al. 2008; Abadi et al. 2010; Tissera et al. 2010; Duffy et al. 2010). However, these simulations generally find that the contraction is weaker than predicted by the Blumenthal et al. (1986) and Gnedin et al. (2004) models. A potentially serious problem with these simulations is they over predict the stellar masses of galaxies, and thus it is not clear how applicable they are to galaxies in the real Universe. More recent simulations, with stronger feedback and hence more realistic stellar to halo mass ratios, report weak contraction or no change in the dark matter mass profiles on MW mass scales (Marinacci et al. 2014; Schaller et al. 2015).

On the scale of dwarf galaxies ($M_{200} \sim 10^{10-11} M_\odot$), a number of different groups have presented fully cosmological hydrodynamical simulations in which the dark matter halo expands (Mashchenko et al. 2008; Governato et al. 2012; Trujillo-Gomez et al. 2015; Chan et al. 2015; Tollet et al. 2016). In these simulations stellar feedback was found to drive rapid (sub-dynamical) time variability of the potential. Dark matter particles orbiting in such a potential gain energy, resulting in halo expansion (Pontzen & Governato 2012). The use of different hydrodynamical codes and sub-grid models suggests that halo expansion is not a numerical artefact, or due to a specific modelling of the subgrid physics.

These apparently conflicting results on dwarf and MW mass scales can be reconciled if the halo response depends, on average, on the halo mass, M_{200} , galaxy stellar mass, M_{star} , or the integrated efficiency of star formation,

$$\epsilon_{\text{SF}} \equiv (M_{\text{star}}/M_{200})/(\Omega_b/\Omega_m). \quad (1)$$

Di Cintio et al. (2014a) found that the inner dark matter density slope, α , was more strongly correlated with ϵ_{SF} , than galaxy or halo mass. At very low efficiencies, there is no change with $\alpha \approx 1.2$ as would be expected. As the star formation efficiency increases, α decreases, reaching $\alpha \approx 0$ at $\epsilon_{\text{SF}} \sim 3\%$. For even higher efficiencies α increases, reaching the CDM value of $\alpha \approx 1.2$ at an efficiency of $\sim 20\%$, and steeper values as high as $\alpha \approx 2$ for efficiencies approaching unity.

Di Cintio et al. (2014b) present a parametrization of the dark matter density profiles in the MaGICC simulations (Stinson et al. 2013), using a five parameter function. As with the inner slope, the other parameters were found to depend on ϵ_{SF} . The goal of this paper is slightly different. Rather than parameterizing the dark matter halo in the hydro simulations, we wish to describe how the dark matter changes [with respect to dark matter-only (DMO) simulations] as a function of the baryonic mass distribution in a galaxy. We also use an order of magnitude more simulations than MaGICC, so we can explore variation of halo response to multiple parameters. Ultimately we want to understand the physical mechanisms that cause contraction and expansion, and to model them. If a physical regularity can be found, it will enable a more general prediction of CDM density profiles in semi-analytic galaxy formation models and when mass modelling galaxy kinematic observations.

This paper is organized as follows. The galaxy formation simulations we use are presented in §2. Changes to the dark matter profiles (between hydrodynamical and dissipationless simulations) are given in §3, including an analytic fitting formula that describes these results in §3.3. §4 presents results for the halo response of our simulations in the context of the

Table 1. Summary of the main differences MUGS, MaGICC and NIHAO simulations, see text for discussion.

name	GASOLINE	cosmology	n_{th} (cm^{-3})	c_*	Δt (Myr)	E_{SN} (10^{51}erg)	ϵ_{ESF}	IMF
MUGS	Wadsley et al. (2004)	WMAP3	0.1	0.05	1.0	0.4	0.0	Kroupa et al. (1993)
MaGICC	Wadsley et al. (2004)	WMAP3	9.3	0.1	0.8	1.0	0.1	Chabrier (2003)
NIHAO	Keller et al. (2014)	Planck	10.6	0.1	0.8	1.0	0.13	Chabrier (2003)

adiabatic contraction formalism, and includes a toy model for halo response involving cycles of inflows and outflows in §4.3. We discuss our results in §5, and give a summary in §6.

2 SIMULATIONS

The galaxies we analyse here come from three projects: Numerical Investigation of a Hundred Astrophysical Objects (NIHAO; Wang et al. 2015), Making Galaxies in a Cosmological Context (MaGICC; Stinson et al. 2013), and McMaster Unbiased Galaxy Simulations (MUGS; Stinson et al. 2010). As described below, NIHAO and MaGICC use a similar star formation and feedback model, and form the ‘correct’ amount of stars. MUGS galaxies are too efficient at forming stars, but we use them as they provide a limiting case for when star formation is very efficient, and they provide a link to similar early simulation works. The main parameters that differ between the simulations are given in Table 1.

All three sets of simulations cover the halo mass range $\sim 10^{10} - 10^{12} M_{\odot}$ at redshift $z = 0$. NIHAO consists of 78 galaxies, MaGICC 11, and MUGS 5. MaGICC and MUGS use the same initial conditions of MW mass haloes, and re-scale them to simulate lower mass galaxies. NIHAO selects haloes to have roughly uniform sampling in log halo mass, and independent of formation history at a given halo mass.

As discussed in previous papers, MaGICC and NIHAO form some of the most realistic simulated galaxies to date, being consistent with a wide range of galaxy properties both in the local and distant universe: evolution of stellar to halo masses and star formation rates (Stinson et al. 2013; Wang et al. 2015); disc sizes (Brook et al. 2012), gas phase metallicities (Obreja et al. 2014); the shape of the MW’s dark matter halo (Butsky et al. 2015); cold and hot gas content (Stinson et al. 2015; Gutcke et al. 2016; Wang et al. 2016); HI sizes and the baryonic Tully-Fisher relation (Brook et al. 2016); stellar disk kinematics (Obreja et al. 2016); shallow inner dark matter density slopes of dwarf galaxies (Tollet et al. 2016); and resolve the ‘too-big-to-fail’ problem of nearby field dwarf galaxies (Dutton et al. 2016). They thus provide plausible, if not unique, templates for how baryonic processes effect the structure of CDM haloes.

2.1 Cosmology

MUGS and MaGICC uses the WMAP3 cosmology (Spergel et al. 2007) with Hubble parameter $H_0 = 73.0 \text{ km s}^{-1} \text{ Mpc}^{-1}$, matter density $\Omega_m = 0.24$, dark energy density $\Omega_{\Lambda} = 1 - \Omega_m = 0.76$, baryon density $\Omega_b = 0.04$ and power spectrum normalization $\sigma_8 = 0.76$, and power

spectrum slope $n = 1$, while NIHAO uses the Planck cosmology (Planck Collaboration et al. 2014): Hubble parameter $H_0 = 67.1 \text{ km s}^{-1} \text{ Mpc}^{-1}$, matter density $\Omega_m = 0.3175$, dark energy density $\Omega_{\Lambda} = 1 - \Omega_m = 0.6825$, baryon density $\Omega_b = 0.0490$, power spectrum normalization $\sigma_8 = 0.8344$, power spectrum slope $n = 0.9624$.

2.2 Hydrodynamics

All three simulation sets use the GASOLINE (Wadsley et al. 2004) smoothed particle hydrodynamics (SPH) code. MUGS and MaGICC use the original version, while NIHAO uses the version of GASOLINE from Keller et al. (2014) that reduces the formation of blobs and improves mixing. Both versions of GASOLINE use the same treatment for cooling via hydrogen, helium, and various metal-lines in a uniform ultraviolet ionizing background as described in Shen et al. (2010).

2.3 Star formation

The simulations use a common recipe for star formation following Stinson et al. (2006), but with three different sets of parameters. Stars form from cool ($T < 15000\text{K}$) dense gas ($n > n_{\text{th}}$). A subset of the particles that pass these criteria are randomly selected to form stars based on the commonly used star formation equation, $\Delta m_*/\Delta t = c_* m_{\text{gas}}/t_{\text{dyn}}$. Here, Δm_* is the mass of the star particle formed, Δt is the time step between star formation events, and c_* is the efficiency of star formation, i.e., the fraction of gas that will be converted into stars during a dynamical time.

In MUGS the threshold density is $n_{\text{th}} = 0.1 \text{ cm}^{-3}$, $c_* = 0.05$, and $\Delta t = 1 \text{ Myr}$. In MaGICC and NIHAO $\Delta t = 0.8 \text{ Myr}$, $c_* = 0.1$ and n_{th} is set to the maximum density at which gravitational instabilities can be resolved $n_{\text{th}} = n_{\text{sph}} m_{\text{gas}}/\epsilon_{\text{gas}}^3$. Here n_{sph} is the number of particles in the SPH smoothing kernel, m_{gas} is the gas particle mass, and ϵ_{gas} is the force softening of the gas particles. The threshold density is 9.3 cm^{-3} in MaGICC and 10.6 cm^{-3} in NIHAO.

2.4 Feedback

The thermal stellar feedback comprises two epochs. The first epoch, ‘early stellar feedback’ (ESF), happens before any supernovae explode. It represents stellar winds and photoionization from the bright young stars. The ESF consists of a fraction ϵ_{ESF} of the total stellar flux being ejected from stars into surrounding gas ($2 \times 10^{50} \text{ erg}$ of thermal energy per M_{\odot} of the entire stellar population). Radiative cooling is left on for the ESF. MUGS does not include ESF (i.e., $\epsilon_{\text{ESF}} = 0$). MaGICC adopts $\epsilon_{\text{ESF}} = 0.10$, which has been tuned to match the evolution of the stellar mass versus halo

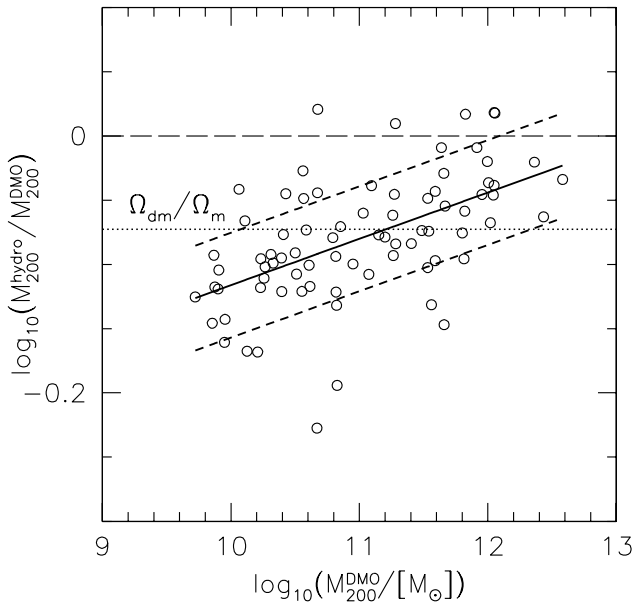


Figure 1. Comparison between halo masses, M_{200} , in hydro and DMO NIHAO simulations. The long-dashed line represents equality, showing that most hydro simulations have lost mass relative to the DMO simulations. In low-mass haloes, the mass-loss is greater than simply failing to accrete or retain the cosmic baryon fraction of mass (dotted line).

mass relation (Behroozi et al. 2013) for a $z = 0$ MW mass galaxy (Stinson et al. 2013). NIHAO adopts $\epsilon_{\text{ESF}} = 0.13$. The slight change is due to the increased mixing, and subsequent higher star formation efficiency, in the upgraded version of GASOLINE used in NIHAO.

The second epoch starts 4 Myr after the star forms, when the first supernovae start exploding. Only supernova energy is considered as feedback in this second epoch. Supernova feedback is implemented using the blastwave formalism described in Stinson et al. (2006). Since the gas receiving the energy is dense, it would quickly be radiated away due to its efficient cooling. For this reason, cooling is delayed for particles inside the blast region for ~ 30 Myr. Stars $8M_{\odot} < m_{\text{star}} < 40M_{\odot}$ eject both energy, E_{SN} , and metals into the interstellar medium gas surrounding the region where they formed. MUGS adopts $E_{\text{SN}} = 4 \times 10^{50}$ erg per SN, and a Kroupa et al. (1993) initial mass function (IMF), while MaGICC and NIHAO adopt $E_{\text{SN}} = 1 \times 10^{51}$ erg, and a Chabrier (2003) IMF. The different IMF and energy per supernova result in a factor of ≈ 5 more energy released per solar mass of stars formed in the MaGICC and NIHAO simulations. This feedback is sufficiently strong to correct the over cooling problem of the MUGS simulations.

2.5 Halo identification

The main haloes in the simulations were identified using the MPI+OpenMP hybrid halo finder AHF¹ (Gill et al. 2004; Knollmann & Knebe 2009). AHF locates local over-densities

¹ <http://popia.ft.uam.es/AMIGA>

in an adaptively smoothed density field as prospective halo centres. The virial masses of the haloes are defined as the masses within a sphere containing $\Delta = 200$ times the cosmic critical matter density, $\rho_{\text{crit}} = 3H(z)^2/8\pi G$.

Each hydrodynamic simulation has a corresponding DMO simulation. We use the superscripts ‘hydro’ and ‘DMO’ to refer to parameters from the hydrodynamical, and DMO simulations, respectively. For example, the halo masses are denoted M_{200}^{hydro} and M_{200}^{DMO} . In general the halo masses for a given initial condition are not identical between the hydro and DMO simulations (Fig. 1). In order for a meaningful comparison between the dark matter haloes profiles we have removed halo pairs with significantly different masses, which for example, occurs when one of the haloes is unrelaxed due to a recent major merger, or when a major merger has not occurred yet in one of the simulations. Loss of gas due to feedback results in a systematic trend with halo mass:

$$\log_{10} \left(\frac{M_{200}^{\text{hydro}}}{M_{200}^{\text{DMO}}} \right) = -0.0447 + 0.0369 \log_{10} \left(\frac{M_{200}^{\text{DMO}}}{10^{12} M_{\odot}} \right), \quad (2)$$

with a scatter of 0.039 dex. Due to these differences, when we calculate quantities at a fraction of the virial radius we pick that of the DMO simulation to ensure that we are using the same physical radius for each simulation pair. Note that the low-mass haloes have lost more mass than simply removing the baryons according to the cosmic baryon fraction (dotted line in Fig. 1), indicating a slowing down of the mass accretion histories of the hydro haloes. Similar results have been found in the APOSTLE simulations of Local Group analogues by Sawala et al. (2016).

3 DARK MATTER PROFILES

3.1 Mass profiles

The dark matter circular velocity profiles, $V_{\text{circ}} = \sqrt{GM(<r)/r}$, for our cosmological simulations are shown in Fig. 2. The radii and velocities have been scaled to the virial radius, R_{200}^{DMO} , and virial velocity, V_{200}^{DMO} , of the DMO simulations. In addition, we have scaled the velocities of the DMO simulations by $\sqrt{1 - f_{\text{bar}}}$, where $f_{\text{bar}} \equiv \Omega_b/\Omega_m$, to approximate the contribution of baryons to the DMO velocity profile. The left-hand panel shows results for the dissipationless simulations, while the right-hand panel shows the results for the hydro simulations. In both panels, the solid lines show simulations from NIHAO, while the dashed lines show simulations from MaGICC and MUGS. These lines are only shown for radii where the circular velocity profile is converged to 10% according to the convergence criteria of Power et al. (2003), modified by Schaller et al. (2015). Dotted lines show the velocity profiles down to the softening length of the dark matter particles, which is typically two to three times smaller than the convergence radius.

As expected, the DMO simulations are well described by the Einasto profile (Einasto 1965),

$$\ln[\rho(r)/\rho_{-2}] = -(2/\alpha)[(r/r_{-2})^{\alpha} - 1], \quad (3)$$

with $\alpha = 0.18$ and concentrations $c \equiv R_{200}/r_{-2} = 6, 10, 16.6$ corresponding to the 2σ range found in large volume N -body simulations (Dutton & Macciò 2014). However, at the

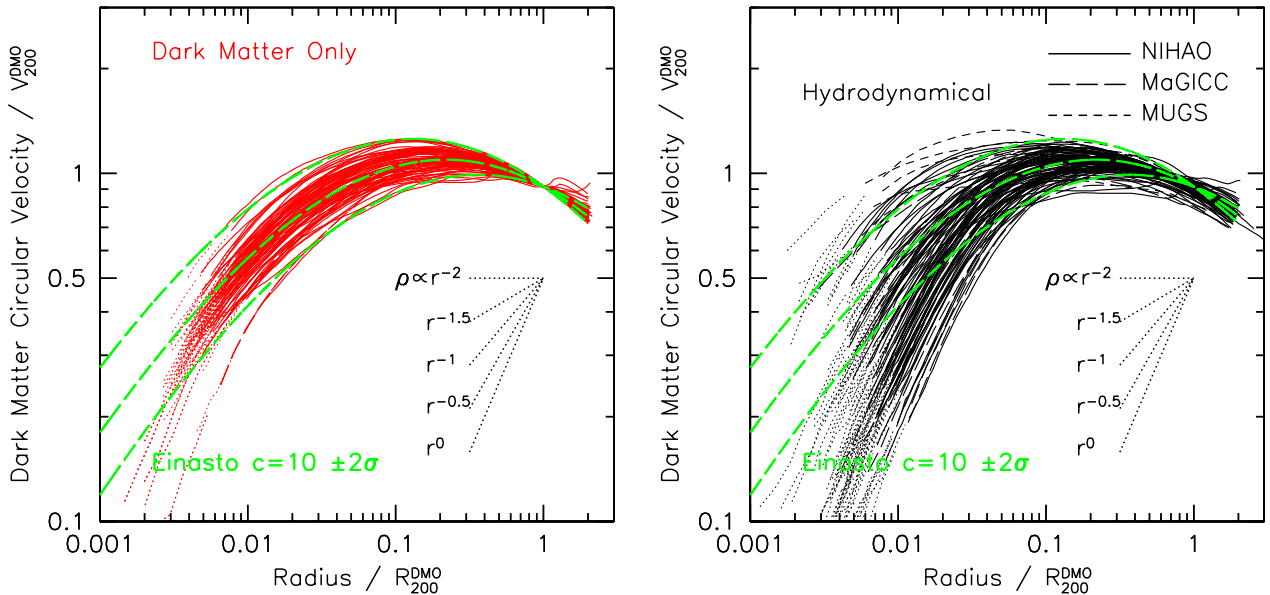


Figure 2. Dark matter circular velocity curves normalized to the virial velocity and virial radius of the DMO simulations. For the DMO simulations we have scaled the velocities by $\sqrt{1 - f_{\text{bar}}}$ to make them directly comparable to the hydrodynamical simulations. Solid and dashed lines show the profiles down to where the velocity profile has converged to 10%, while the dotted lines continue the profile to the dark matter softening length. Hydro simulations (right-hand panel) show a much larger spread in rotation curve shapes than the DMO simulations (left-hand panel). For reference, Einasto profiles with concentration $c = 6, 10, 16.6$ (the 2σ range) and $\alpha = 0.18$ are shown (long-dashed green). Circular velocity slopes for various power-law density profiles (black dotted) show that the hydro simulations can have both steeper and shallower density profiles than those found in DMO simulations.

smallest resolved radii many of the hydro simulations have dark matter density profiles with inner slopes shallower than the nominal CDM value of r^{-1} . There is also clearly a much wider range in dark matter profiles in the hydro simulations. For example, at 1% of the virial radius, the DMO simulations show an absolute variation in dark matter circular velocity of just a factor of 2, whereas the hydro simulations show an order of magnitude spread.

3.2 Halo response to galaxy formation

The change in dark matter profiles is shown more clearly in Fig. 3. The y -axis shows the ratio between the dark matter circular velocity in the hydro simulations, $V_{\text{dark}}^{\text{hydro}}(r)$, to that in the DMO, $V_{\text{dark}}^{\text{DMO}}(r)$, simulations. The DMO velocities have been scaled by a factor of $\sqrt{1 - f_{\text{bar}}}$ so that a ratio of 1 implies no change in the dark matter mass profile. The mass ratio is thus $[V_{\text{dark}}^{\text{hydro}}(r)/V_{\text{dark}}^{\text{DMO}}(r)]^2$. For a power-law density profile $\rho \propto r^{-1}$ the enclosed mass goes like $M(r) \propto r^2$, and thus the velocity ratio roughly corresponds to the radial expansion (or contraction factor). For example, a velocity ratio of 0.5 means shells of dark matter have expanded a factor of ~ 2 .

The solid lines show simulations from NIHAO, while the dashed lines show simulations from MaGICC and MUGS. The points show the location of the 3D half-mass radius of the stars: NIHAO (circles), MaGICC (squares), and MUGS (triangles). The MaGICC and NIHAO simulations span a similar range of halo response, while the MUGS simulations are among the most contracted. Amongst other things, this shows that the role of the hydrodynamics (which has been

improved in NIHAO versus MaGICC) plays a subdominant role to the strength of the feedback.

Changes are larger at smaller radii, both when the haloes expand and contract. At radii greater than 10% of the virial radius, there is little change in the dark matter profile. This is to be expected, since the half-mass radii of the stars are typically between 0.5 and 5 per cent of the virial radius. At these scales, where baryons condense and stars form, there is a wide range of halo responses. At 1% of the virial radius the halo circular velocity increases and decreases by up to factor of ~ 2.5 , corresponding to a change in enclosed mass by a factor of ~ 6 . Clearly, baryons can have a major impact on the structure of the dark matter halo.

This plot also highlights the importance of spatial resolution. In order to see significant expansion or contraction, simulations need to be able to resolve scales significantly smaller than $\sim 5\%$ of the virial radius. Our simulations resolve $\sim 1\%$ of the virial radius across three decades in halo mass. However, large volume simulations such as EAGLE (Schaye et al. 2015) and ILLUSTRIS (Vogelsberger et al. 2014) only have sufficient resolution for haloes of MW mass and above.

Using the MaGICC and MUGS simulations, Di Cintio et al. (2014a) found that the logarithmic slope of the dark matter density profile measured between 1 and 2% of the virial radius was correlated with the efficiency of star formation, $\epsilon_{\text{SF}} = (M_{\text{star}}/M_{200})/(\Omega_{\text{b}}/\Omega_{\text{m}})$. Thus, we colour code the lines in Fig. 3 according to ϵ_{SF} . We identify four qualitative behaviours in the halo response:

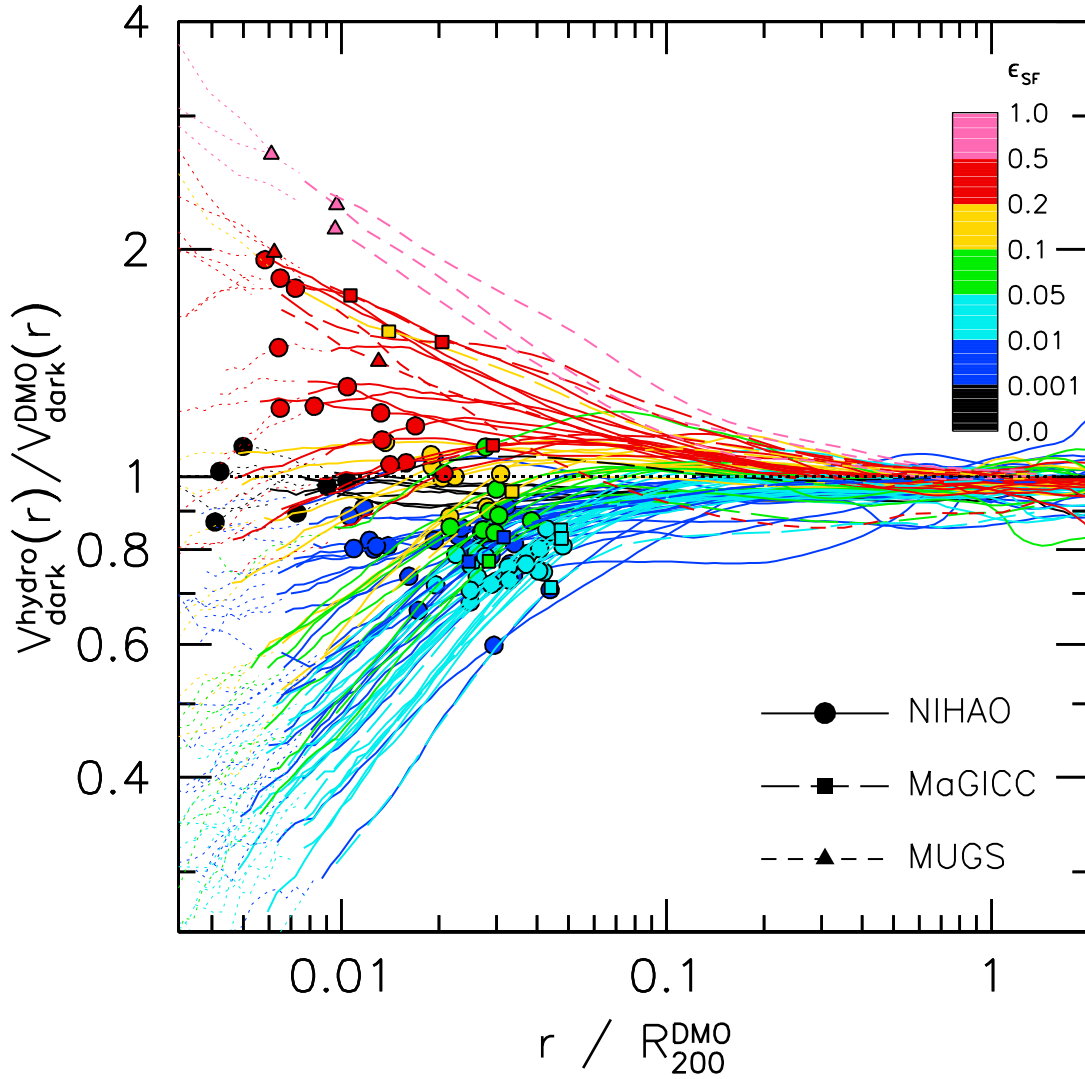


Figure 3. Ratio between dark matter circular velocity curves from the hydro $V_{\text{dark}}^{\text{hydro}}(r)$ and dissipationless $V_{\text{dark}}^{\text{DMO}}$ simulations. Points show the location of stellar half-mass radii, with different symbols for the NIHAO (circles), MaGICC (squares), and MUGS (triangles) simulations. Colours corresponds to integrated star formation efficiency, $M_{\text{star}}/M_{200}/f_{\text{bar}}$, as indicated.

- (A) no change in the dark matter profile ($\epsilon_{\text{SF}} \lesssim 10^{-3}$).
- (B) expansion at all radii, with more expansion at smaller radii ($10^{-3} \lesssim \epsilon_{\text{SF}} \lesssim 0.1$) and a maximum expansion for $\epsilon_{\text{SF}} \sim 0.03$.
- (C) contraction at large radii with a maximum near $0.05R_{200}$, together with expansion at small radii ($0.1 \lesssim \epsilon_{\text{SF}} \lesssim 0.2$).
- (D) contraction at all radii with more contraction at smaller radii ($\epsilon_{\text{SF}} \gtrsim 0.2$).

Observational estimates from halo abundance matching and weak gravitational lensing find the maximum $\epsilon_{\text{SF}} \sim 0.25$ at a halo mass of $\sim 10^{12}M_{\odot}$ (e.g., [Conroy & Wechsler 2009](#); [Moster et al. 2010](#); [Leauthaud et al. 2012](#); [Hudson et al. 2015](#)). Thus case (D) is likely to occur at the peak of star formation efficiency. Since there is a scatter of ~ 0.2 dex in stellar mass at fixed halo mass ([More et al. 2011](#); [Behroozi et al. 2013](#); [Reddick et al. 2013](#)), galaxies with $\epsilon_{\text{SF}} > 0.2$ are also

possible in haloes above and below $M_{200} \sim 10^{12}M_{\odot}$ that scatter up in efficiency. The MW is an example of a galaxy with a high star formation efficiency of $\epsilon_{\text{SF}} \simeq 0.30$. Galaxies with very efficient star formation $\epsilon_{\text{SF}} \gtrsim 0.5$ are also possible with 2σ deviations in $M_{200} \sim 10^{12}M_{\odot}$ haloes, so that even the ‘overcooled’ simulations from MUGS may provide a template for a subset of the galaxy population. At the low mass end of our simulations, haloes of mass $M_{200} = 10^{10}M_{\odot}$ are expected to host galaxies of stellar mass $\sim 10^6$ so that $\epsilon_{\text{SF}} \sim 10^{-3}$. The scatter in ϵ_{SF} is quite possibly very large in these low mass haloes ([Wang et al. 2015](#); [Garrison-Kimmel et al. 2016](#)) and thus we expect some low-mass haloes to show no change (case A), while others expansion (case B).

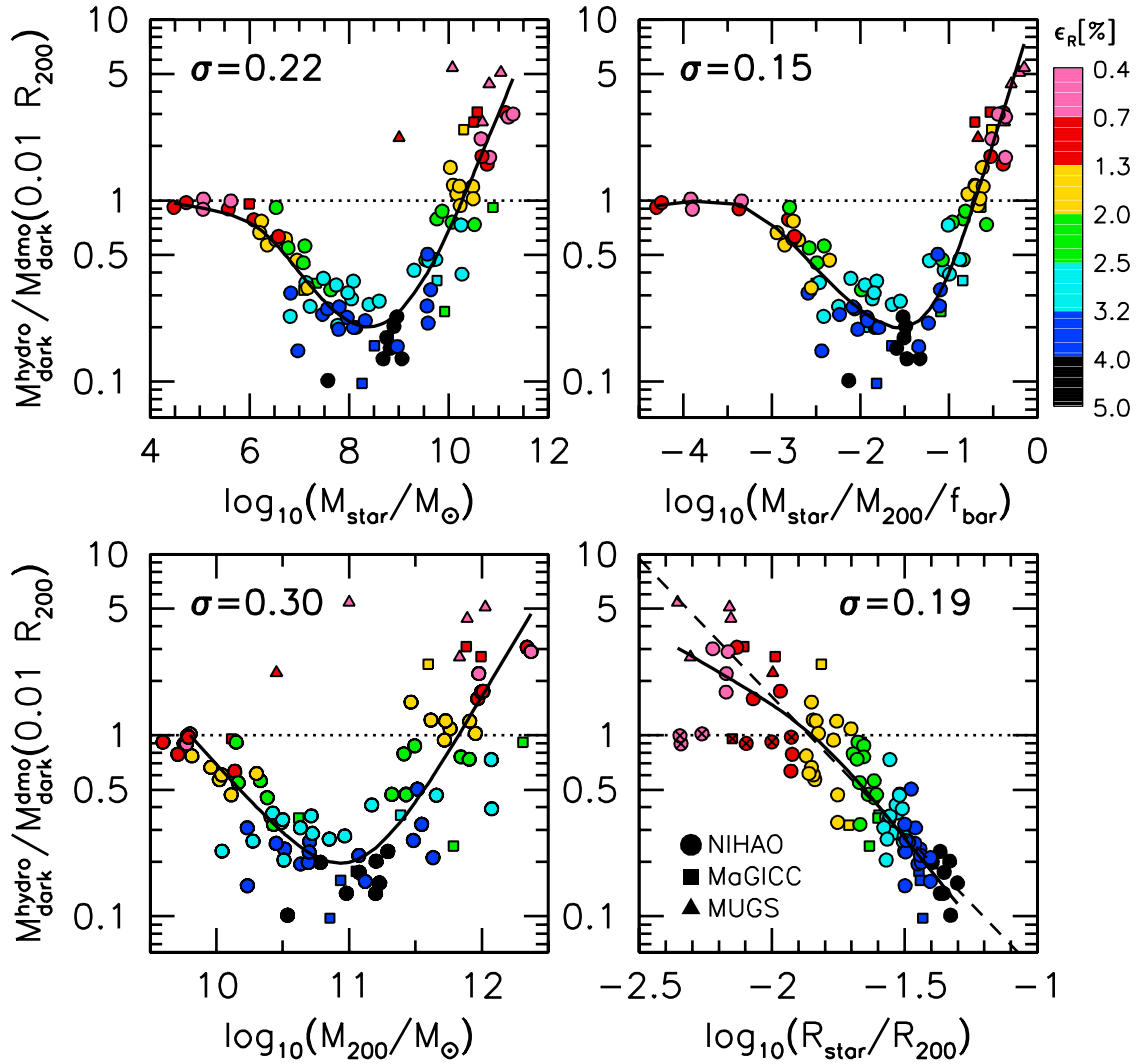


Figure 4. Halo response at 1 per cent of the virial radius (expressed in terms of the dark matter mass ratio) versus halo mass M_{200} (bottom left), stellar mass M_{star} (top left), integrated star formation efficiency $M_{\text{star}}/M_{200}/f_{\text{bar}}$ (top right), and galaxy contraction factor $\epsilon_{\text{R}} = r_{1/2}/R_{200}$ (bottom right). Points are colour coded by ϵ_{R} . At fixed halo mass, stellar mass, and star formation efficiency we see a trend for smaller galaxies to have more contraction / less expansion. Point types correspond to the different simulation sets: NIHAO (circles), MaGICC (squares), MUGS (triangles).

3.3 Correlations between halo response and galaxy parameters

To show the trend with ϵ_{SF} more explicitly, Fig. 4 shows the dark matter mass ratio (\equiv dark matter velocity ratio squared) measured at 1 per cent of the virial radius versus ϵ_{SF} as well as halo mass, M_{200} , stellar mass, M_{star} , and the compactness parameter, $\epsilon_{\text{R}} = r_{1/2}/R_{200}$, the ratio between the 3D stellar half-mass size and halo virial radius. For each relation the solid line shows a spline interpolated median, and the overall standard deviation about each relation is given. Of these four fundamental parameters star formation efficiency is the best predictor of halo response ($\sigma = 0.15$), followed by compactness ($\sigma = 0.19$), stellar mass ($\sigma = 0.21$) and halo mass ($\sigma = 0.29$).

Even though there are clear trends with stellar and halo

mass in the NIHAO (circles) and MaGICC (squares) simulations, the MUGS simulations (triangles) show that stellar or halo mass by themselves are not the driving parameters for halo response. The two lowest mass MUGS simulations have halo masses of $M_{200} \approx 10^{10.5}$ & $10^{11} M_{\odot}$ and strongly contracted haloes. At these mass scales the NIHAO simulations have the opposite halo response, i.e., strong expansion. Likewise the stellar masses in the MUGS simulations are $M_{\text{star}} \approx 10^9$ & $10^{10} M_{\odot}$. At these mass scales, the NIHAO simulations have a factor of 5 lower dark halo masses within 1% of the virial radius. By contrast, when we look at the star formation efficiency (upper-right panel), the MUGS and NIHAO simulations follow the same relation.

From a theoretical point of view, one would expect that the halo response would depend not just on global properties, such as M_{star}/M_{200} , but on local ones, such as the dis-

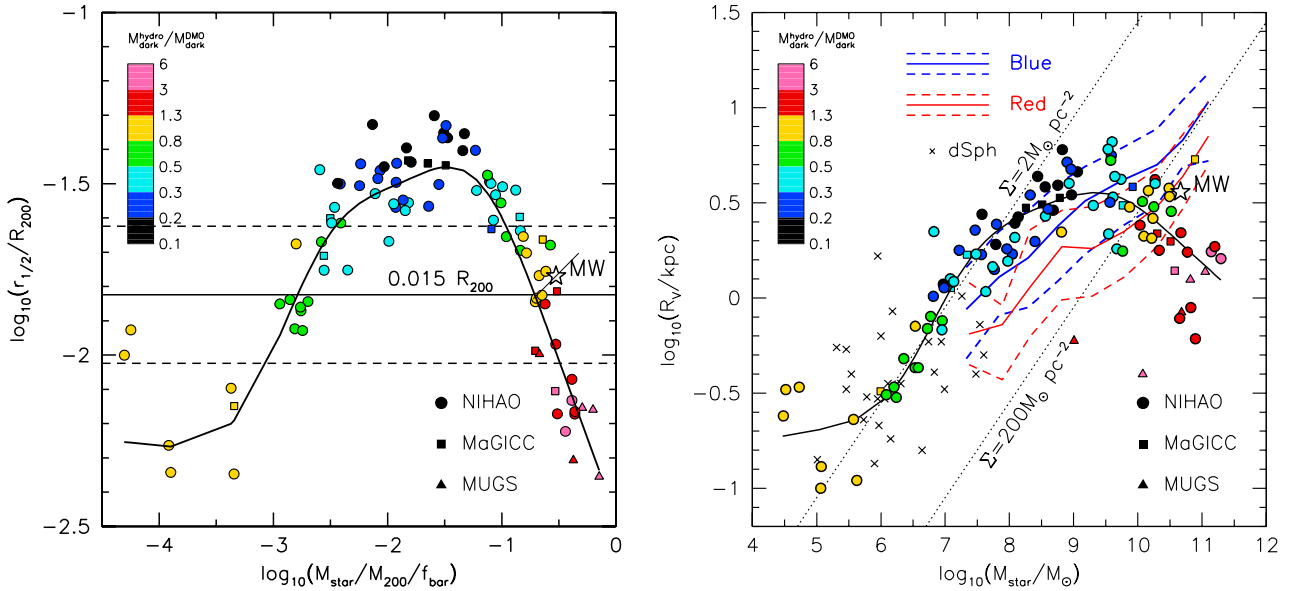


Figure 5. Halo response in the size versus stellar mass plane, using physical units (right) and relative to the halo size and mass (left). The left-hand panel uses the 3D stellar half-mass radii, $r_{1/2}$, while the right panel uses the more directly observable 2D stellar half-light radii in the V band, R_V . Coloured points show simulated galaxies from NIHAO (circles), MaGICC (squares), and MUGS (triangles). Points are colour coded by the halo response, defined to be the dark matter mass ratio between hydro and DMO simulations at 1% of the virial radius. In the left-hand panel, the solid and dashed lines show $r_{1/2} = 0.015R_{200} \pm 0.2$ dex derived by Kravtsov (2013) using halo abundance matching. In the right-hand panel, we include observations of 2D half-light radii from Baldry et al. (2012). Red and blue galaxies are shown with correspondingly coloured lines (median together with 16th and 84th percentiles), dwarf spheroidal (dSph) galaxies are shown with black crosses. The star shows the MW. For reference, the black dotted line show lines of constant effective surface density of $\Sigma = 2M_{\odot}\text{pc}^{-2}$ and $\Sigma = 200M_{\odot}\text{pc}^{-2}$.

tribution of the baryons. In the adiabatic contraction formalism (Blumenthal et al. 1986) and its variants (Gnedin et al. 2004; Abadi et al. 2010; Dutton et al. 2015), at a fixed halo and stellar mass, more compact baryon distributions result in more contraction. For the expansion case the stars are collisionless, so they are expected to expand with the dark matter. Thus an expanded stellar distribution is a signature of dark halo expansion.

The lower-right panel of Fig. 4 indeed shows a strong correlation between the compactness of the stellar distribution, ϵ_R and the halo response, with more extended stellar distributions having stronger expansion. The points in all four panels are colour coded by ϵ_R . This shows that at fixed halo mass, stellar mass, and star formation efficiency, smaller galaxies have more contraction and larger galaxies have more expansion. This correlation fails to hold for the no-change case at low stellar masses/star formation efficiencies ($\epsilon_{\text{SF}} \lesssim 10^{-3}$). Excluding these (marked with an x) and fitting a straight line gives

$$y = -0.28(\pm 0.11) - 1.52(\pm 0.42)(x + 1.68) \quad (4)$$

where $y = \log_{10}(M_{\text{dark}}^{\text{hydro}}/M_{\text{dark}}^{\text{DMO}})$, and $x = \log_{10}(r_{1/2}/R_{200})$. The scatter about this relation is $\sigma = 0.17$. Thus including the distribution of the stars should improve the predictive power of a halo response model based on global galaxy and halo parameters.

3.4 Halo response as a function of star formation efficiency and galaxy compactness

To determine the relative importance of star formation efficiency, and galaxy compactness, Fig. 5 shows correlations between size, stellar mass, and halo response. Here, the halo response is defined as the dark matter mass ratio at 1 per cent of the virial radius. The left-hand panel shows the relation between ϵ_R and ϵ_{SF} with points colour coded according to the halo response. The right-hand panel shows the directly observable (2D half-light) size versus stellar mass. In both panels, we show the MW using a disk scalelength of $R_d = 2.15$ ($r_{1/2} \sim 3.6$) kpc and $M_{\text{star}} = 4.6 \times 10^{10}M_{\odot}$ from Bovy & Rix (2013) and a halo mass of $M_{200} = 10^{12}M_{\odot} \pm 0.2$ dex (Peñarrubia et al. 2016, and references therein). In the left-hand panel, we show $r_{1/2} = 0.015R_{200} \pm 0.2$ dex derived by Kravtsov (2013) using halo abundance matching. In the right-hand panel, we show observations of 2D half-light radii for red, blue, and dSph galaxies from Baldry et al. (2012).

Interestingly, galaxies with similar halo response fall in similar parts of the parameter space. As we saw in Fig. 4 at fixed ϵ_{SF} , there is a clear trend for larger galaxies (at fixed star formation efficiency or mass) to have more expanded haloes, and smaller galaxies to have more contracted haloes. However, at a fixed ϵ_R (or size) there are two branches with different ϵ_{SF} (or mass) for the same halo response. Thus neither compactness nor star formation efficiency alone determines the halo response.

If we fit lines to haloes of similar response where there

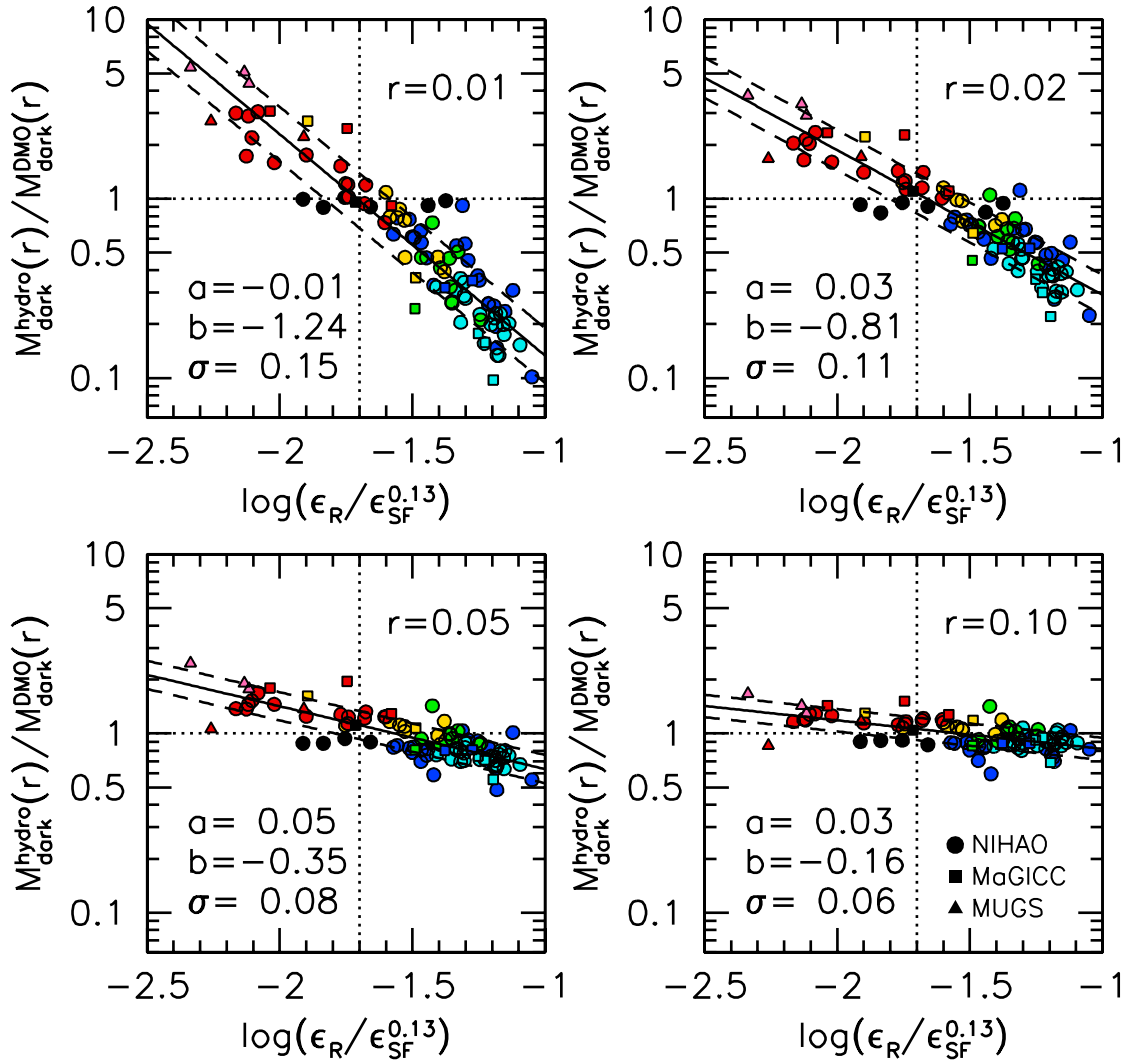


Figure 6. Halo response at 1, 2, 5, and 10 per cent of the virial radius versus $\epsilon_R/\epsilon_{\text{SF}}^{0.13}$. At all radii, the relation is well fitted with a power law. Point types are as in previous figures: NIHAO (circles); MaGICC (squares); MUGS (triangles).

is a significant baseline, we find slopes of ~ 0.13 for ϵ_R versus ϵ_{SF} and ~ 0.2 for R_V^{2D} versus M_{star} . Constant surface density [$\Sigma = M_{\text{star}}/(2\pi R_V^2)$] has a slope of 0.5 in the R_V versus M_{star} plane, and thus the density of stars is not a more fundamental parameter. This is clearly seen for dwarf galaxies, which have roughly constant surface density of $\Sigma = 2M_{\odot}\text{pc}^{-2}$, while the halo response varies from no change at low stellar masses ($\sim 10^6 M_{\odot}$) to expansion at high stellar masses ($\sim 10^8 M_{\odot}$).

Taking out these trends, Fig. 6 shows the halo response measured at various radii versus $\epsilon_R/\epsilon_{\text{SF}}^{0.13}$. At all radii, r , the relation is well fitted with a power law in $M_{\text{dark}}^{\text{hydro}}(r)/M_{\text{dark}}^{\text{DMO}}(r)$ versus $\epsilon_R/\epsilon_{\text{SF}}^{0.13}$ space. The slope, b , zero-point, a , and scatter, σ , of this correlation depends on the radius where the mass ratio is measured, r . Thus, the following equation describes the halo response at any radius

as a function of ϵ_R and ϵ_{SF} :

$$\log_{10} \left[\frac{M_{\text{dark}}^{\text{hydro}}(r)}{M_{\text{dark}}^{\text{DMO}}(r)} \right] = a(r) + b(r) [\log_{10} (\epsilon_R/\epsilon_{\text{SF}}^{0.13}) - 1.7]. \quad (5)$$

The dependence of a , b , and σ , with radius are shown in Fig. 7. We fit the relations with the following functions. A double power-law with slopes s_1 and s_2 :

$$D(x, x_0, y_0, s_1, s_2, t) = y_0 + s_1(x - x_0) + \frac{(s_2 - s_1)}{t} \log_{10} \left\{ \frac{1}{2} + \frac{1}{2} [10^{(x-x_0)^t}] \right\}, \quad (6)$$

and a sigmoid function which smoothly varies between a y -value of y_1 and y_2 :

$$S(x, x_0, y_1, y_2, t) = y_2 + \frac{y_1 - y_2}{1 + (10^{(x-x_0)^t})}. \quad (7)$$

The slope as a function of radius, $b(r)$, is given by

$$b(r) = D[\log_{10}(r), -1.1, -0.2, 1.35, 0.0, 2.0], \quad (8)$$

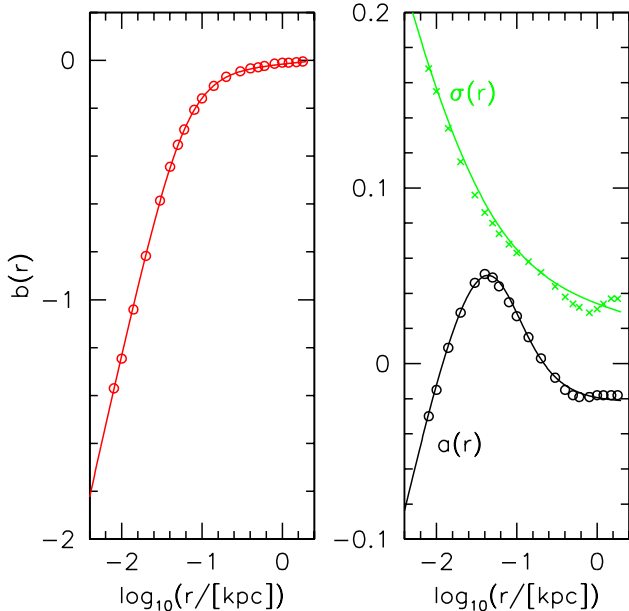


Figure 7. The halo response, $M_{\text{dark}}^{\text{hydro}}/M_{\text{dark}}^{\text{DMO}}(r)$, at each radius, r , is fitted with equation (5). The left-hand panel shows the slope, $b(r)$, while the right-hand panel shows the normalization, $a(r)$, and scatter, $\sigma(r)$. The solid lines show our fitting formula.

the zero-point as a function of radius, $a(r)$, is given by

$$a(r) = D[\log_{10}(r), -0.15, 0.085, 1.5, 0.0, 2.0] + S[\log_{10}(r), -1.0, 0.0, -0.13, 2.0] \quad (9)$$

and the 1σ scatter is given by

$$\sigma(r) = D(\log_{10}(r), -1.1, 0.65, -1.4, 0.0, 1.0). \quad (10)$$

These predictions break down at low star formation efficiencies ($\epsilon_{\text{SF}} \lesssim 0.001$), so we apply an S-function to the halo response (equation 5) and the scatter (equation 10) with $S[\log_{10}(\epsilon_{\text{SF}}), -3, 0, 1, 2]$. This function asymptotes to zero as $\epsilon_{\text{SF}} \rightarrow 0$, so we add in quadrature a scatter of 0.03 dex.

Fig. 8 shows a comparison between the halo response in the NIHAO simulations (solid black lines) and that predicted by our analytical fit (dashed line and shaded region) for a representative sub-sample of haloes. Reassuringly the model, which was calibrated against these simulations, does indeed recover the diversity of halo responses.

3.5 Implications

If this halo response model holds outside the range of ϵ_{R} and ϵ_{SF} where we have simulations, then there are some interesting implications. Fig. 5 shows that our simulations do not cover the full range of observed galaxies in the size versus mass plane. At stellar masses between $\sim 10^7$ and $10^9 M_{\odot}$ our simulations lack small galaxies, while at high masses $\sim 10^{11} M_{\odot}$ our simulations lack large galaxies. Part of this discrepancy is due to low mass red galaxies preferentially being satellites, whereas all the NIHAO galaxies we show are centrals. Comparing to the just observed blue galaxies, the NIHAO simulations are offset high by $\sim 1\sigma$ at a stellar

mass of $\sim 10^8 M_{\odot}$, and offset low by $\sim 1\sigma$ at a stellar mass of $\sim 10^{10} M_{\odot}$. The small half-light sizes can be traced to overly compact bulges, rather than the discs being too small. We note that a similar feature is seen in the EAGLE simulations (Crain et al. 2015) with constant stellar feedback efficiency (as we adopt here). Their solution is to increase the efficiency of the stellar feedback in dense gas, and to decrease the efficiency in low-density gas, to correct for numerical radiative energy losses. Even though our massive galaxies are smaller than typical observed galaxies, they actually overlap with the MW, which is known to be atypically small (Hammer et al. 2007).

The slope of the size-mass relation is roughly the same as the slope of constant halo response, i.e., ~ 0.2 . Thus, we would predict that a typical spiral galaxy (with $M_{\text{star}} \gtrsim 10^8 M_{\odot}$) would have mild halo expansion, a galaxy offset by 1σ to large sizes would have strong expansion, while a 1σ small galaxy (e.g., the MW) would have no change. A typical bulge-dominated galaxy would also have no change in the dark matter halo. This is in contrast to the strong mass dependence found in the NIHAO and MaGICC simulations here and in previous works (Di Cintio et al. 2014a,b; Tollet et al. 2016). The strong mass dependence can be traced to the strong dependence of compactness with star formation efficiency.

4 TOWARDS A PHYSICAL MODEL FOR HALO RESPONSE

We now turn our attention to a physical model for the response of CDM haloes to baryonic galaxy formation processes. A more elaborate analysis of this toy model is given in Dekel et al. (in preparation).

4.1 Adiabatic contraction formalism

Given a spherically enclosed mass profile from a DMO simulation, $M_i(r)$, (where the i refers to initial), we wish to derive the final dark matter profile, $M_{\text{dm},f}(r)$, once the final baryonic mass profile, $M_{\text{b},f}(r)$, is specified. It is assumed the initial mass profile is split into baryons and dark matter according to the cosmic baryon fraction: $M_{\text{b},i}(r) = f_{\text{bar}} M_i(r)$, and $M_{\text{dm},i}(r) = (1 - f_{\text{bar}}) M_i(r)$.

The standard model of halo response is adiabatic contraction introduced by Blumenthal et al. (1986). As well as adiabatic invariance, this model assumes spherical symmetry, homologous contraction, and circular particle orbits, resulting in conservation of the angular momentum and thus $rM(r) = \text{const}$, where $M(r)$ is the total mass enclosed within radius r . Additionally assuming the dark matter shells do not cross: $M_{\text{dm},f}(r_f) = M_{\text{dm},i}(r_i)$, where r_i is the ‘initial’ radius of a shell of dark matter, and r_f is the ‘final’ radius of this shell after the effects of baryonic processes are included, yields

$$r_f/r_i = M_i(r_i)/[M_{\text{b},f}(r_f) + M_i(r_i)(1 - f_{\text{bar}})]. \quad (11)$$

Thus given M_i and $M_{\text{b},f}$, one can solve equation (11) for the mapping between r_f and r_i , and hence derive the final dark matter profile.

An example of how the radii and masses are calculated in one of our simulations is shown in Fig. 9. The solid

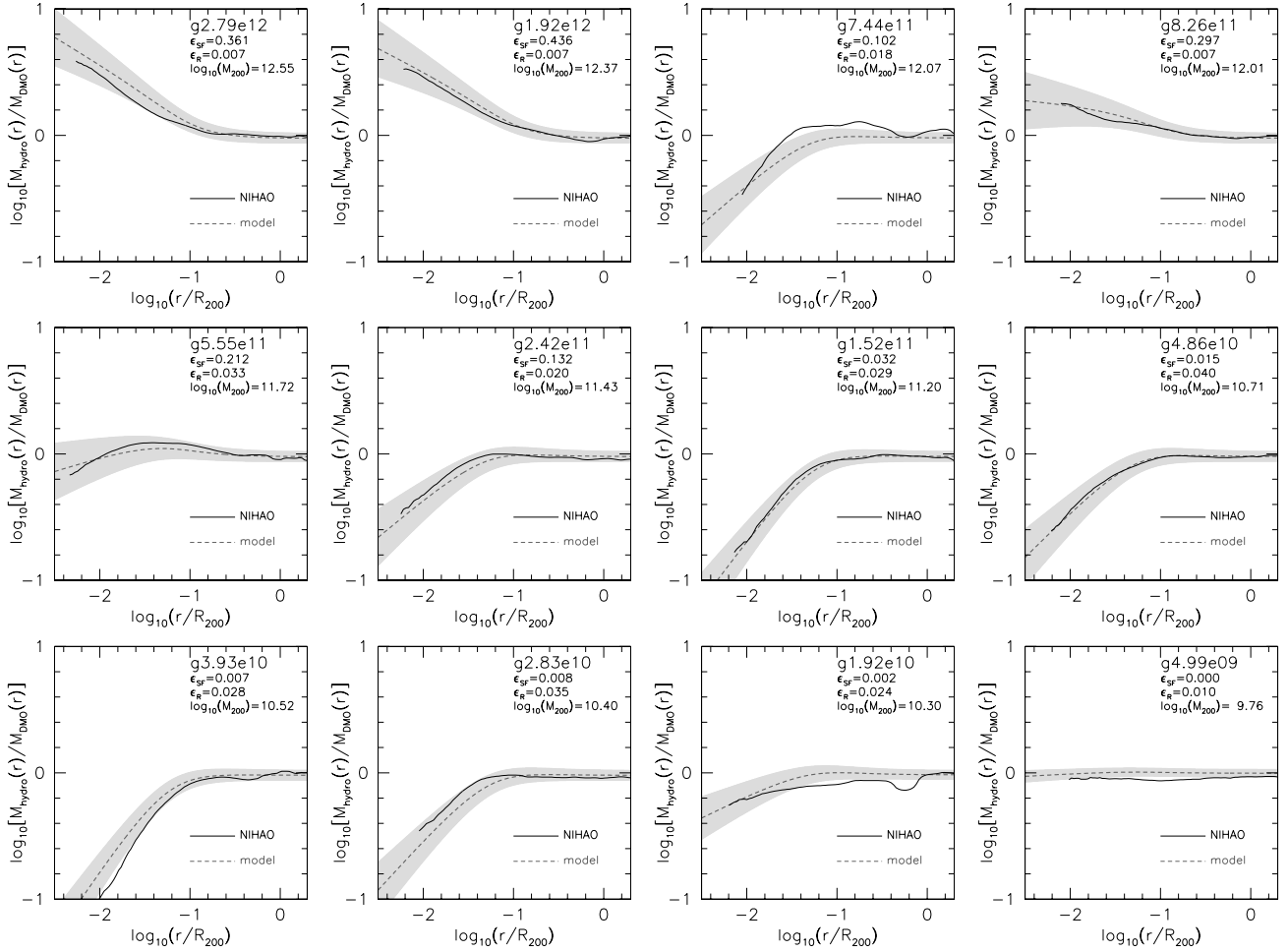


Figure 8. Predicted change (dashed lines) with 1σ uncertainty (shaded region) versus actual change in dark halo mass profiles (solid black lines) for a representative subset of NIHAO galaxies ordered by halo mass from upper left to lower right. In each panel, the galaxy ID, star formation efficiency, compactness parameter, and halo masses are given.

lines show the total (black), dark matter (red), and baryonic (blue) mass profiles for the hydro simulation for halo mass $8.26e11$. The dashed lines show the total (black) and implied dark matter (red) mass profiles for the corresponding dark matter only (DMO) simulation. The horizontal dotted green line shows an arbitrary mass, which intersects the hydro (‘final’) dark matter mass profile at r_f and the DMO (‘initial’) dark matter mass profile at r_i . M_f and M_i are then the total enclosed mass at r_f and r_i , respectively. The arbitrary mass is varied from the smallest resolved to the virial mass to obtain a profile of r_f/r_i and M_i/M_f . We can then compare the relation between r_f/r_i and M_i/M_f from the simulations to test the adiabatic contraction model.

4.2 Halo response in NIHAO simulations

Fig. 10 shows the tracks of our simulations in the r_f/r_i versus M_i/M_f plane. The results from each simulation pair are colour coded by the star formation efficiency, and are plotted down to the convergence radius of the DMO simulation. The y -axis shows the ‘contraction’ factor, while the x -axis can (typically) be mapped monotonically to radius. The adiabatic contraction formula (Eq. 11) predicts that

$r_f/r_i = M_i/M_f$, which is indicated by the diagonal dotted line in the figure. No change in the dark matter profile corresponds to the horizontal dotted line at $r_f/r_i = 1$.

The first point that is apparent from Fig. 10 is that the halo response is not adiabatic in any of our simulations, confirming previous studies (Gnedin et al. 2004; Abadi et al. 2010; Pedrosa et al. 2010; Dutton et al. 2015). The second point is that the halo response does not follow a single track. However, in contrast to these studies, which found only contraction with a mild variation in the halo response, our simulations show a much wider diversity of halo responses, including expansion. As expected from Fig. 3 the halo response is strongly correlated with the star formation efficiency. This is more clearly shown in Fig. 11, which shows the halo response for NIHAO haloes (solid lines) binned by star formation efficiency. Here, the lines are plotted from $0.01 R_{200}$ to R_{200} .

The deviation from adiabatic contraction is increasing with decreasing ϵ_{SF} : haloes with lower star formation efficiency have higher r_f/r_i (i.e., less contraction / more expansion) at fixed M_i/M_f . The long-dashed lines in the left panel of Fig. 11 show the halo response predicted by the Gnedin et al. (2004) model. This model results in weaker

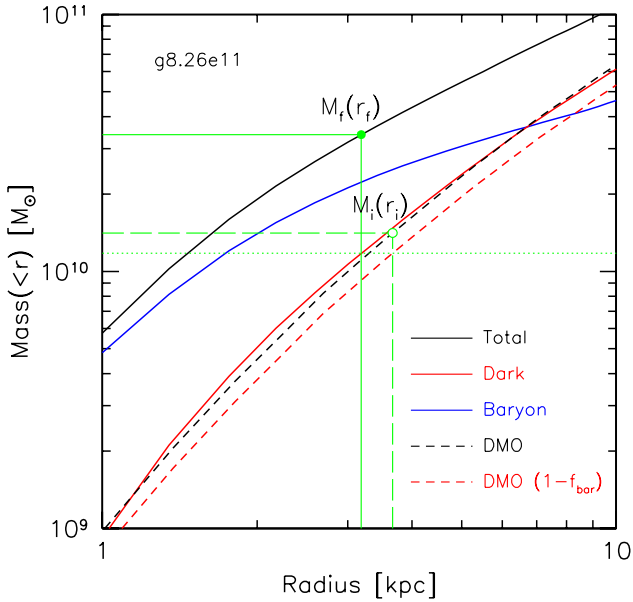


Figure 9. Example showing how r_f, r_i, M_f, M_i are calculated in (a portion of) the cumulative mass vs radius plot for simulation g8.26e11. The horizontal green dotted lines shows an arbitrary mass, here $10^{10.07} M_\odot$. The radius this intersects the dark matter profile from the hydro simulation is termed r_f (vertical green solid), while the radius this intersects the dark matter profile from the DMO simulation is termed r_i (vertical green dashed). The total masses contained within r_f and r_i are then given by M_f (horizontal green solid) and M_i (horizontal green dashed) respectively.

contraction for lower ϵ_{SF} galaxies, and even mild expansion for very low ϵ_{SF} , however, for all star formation efficiencies this model over predicts the contraction. The discrepancy is largest for low M_i/M_f (i.e., small radii). The short-dashed lines show the model of [Abadi et al. \(2010\)](#), which has a fixed path in the halo response plane. This model is close to our simulation results at $\epsilon_{\text{SF}} \sim 0.4$, but fails to match lower ϵ_{SF} haloes.

The dotted lines in the right-hand panel show tracks of $r_f/r_i = (M_i/M_f)^\nu$ for various values of ν . This formula is useful in semi-empirical galaxy formation models ([Dutton et al. 2007](#)) and rotation curve mass models ([Dutton et al. 2013a](#)), as with a single parameter, ν , one can smoothly vary between adiabatic contraction ($\nu = 1$), no change ($\nu = 0$), and expansion ($\nu < 0$). However, despite its flexibility, this function does not capture the diversity of halo response seen in our simulations. It only reliably recovers the halo response for $\epsilon_{\text{SF}} \sim 0.03$, furthermore, it lacks a direct physical interpretation. This failure of previous models and fitting formulae motivates us to derive a new toy model for the halo response.

4.3 Toy model for halo contraction and expansion

We now discuss a toy model for halo response that will be useful for guiding the discussion of the physical mechanisms at play. We emphasize here that we employ an isolated shell toy model, which is a crude simplification. An analysis for

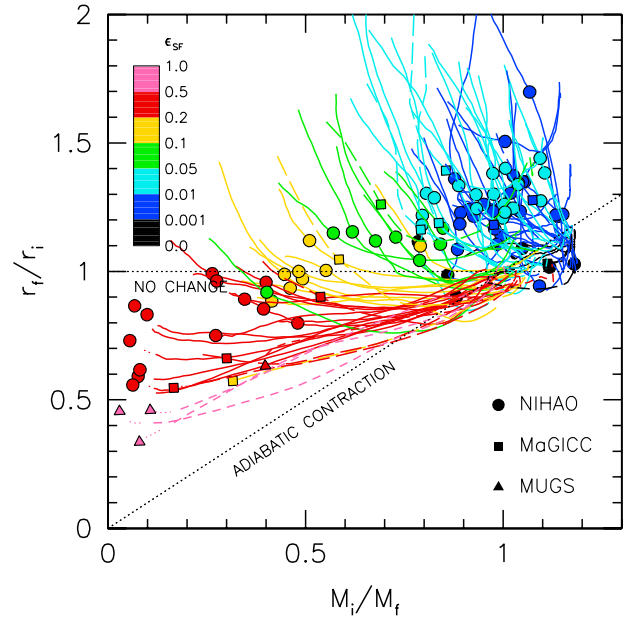


Figure 10. Halo response is not adiabatic, nor does it follow a universal path in the radius versus mass plane. Rather, the path is correlated with the star formation efficiency, ϵ_{SF} . Each line shows a different dark matter halo. Lines are colour coded by star formation efficiency (as indicated).

a full halo density profile and the error made by the shell approximation is given in [Dekel et al. \(in preparation\)](#).

We consider two physical processes that change the dark halo structure: *adiabatic inflow* of gas and *impulsive outflow* of gas. [Fig. 12](#) shows a variety of cases: pure outflow (upper left); net outflow (upper middle); equal inflow and outflow (upper right); pure inflow (lower left); and net inflow (lower middle and right). [Fig. 13](#) shows the paths of these models, using the same colour scheme, in the classical halo response plane: r_f/r_i versus M_i/M_f .

4.3.1 Adiabatic inflow

Consider a spherical shell of mass $(1 - f_{\text{in}})M$ and radius r_i , with circular orbits. Assume that gas of mass $f_{\text{in}}M$ infalls adiabatically into the shell center. The total mass is now M . Using the adiabatic invariant, it is known that the shell contracts to a new radius, r_a , that is inversely proportional to the mass ratio ([Blumenthal et al. 1986](#)):

$$\frac{r_a}{r_i} = (1 - f_{\text{in}}), \quad \frac{M_a}{M_i} = \frac{1}{(1 - f_{\text{in}})}. \quad (12)$$

4.3.2 Impulsive outflow

Assume that gas of mass $f_{\text{out}}M$ is removed instantaneously from the centre of the sphere. In the impulse approximation, the instantaneous velocities remain as they were prior to the outflow:

$$V_a^2 = GM/r_a, \quad (13)$$

namely the system is temporarily out of virial equilibrium. The total energy (potential plus kinetic) immediately after

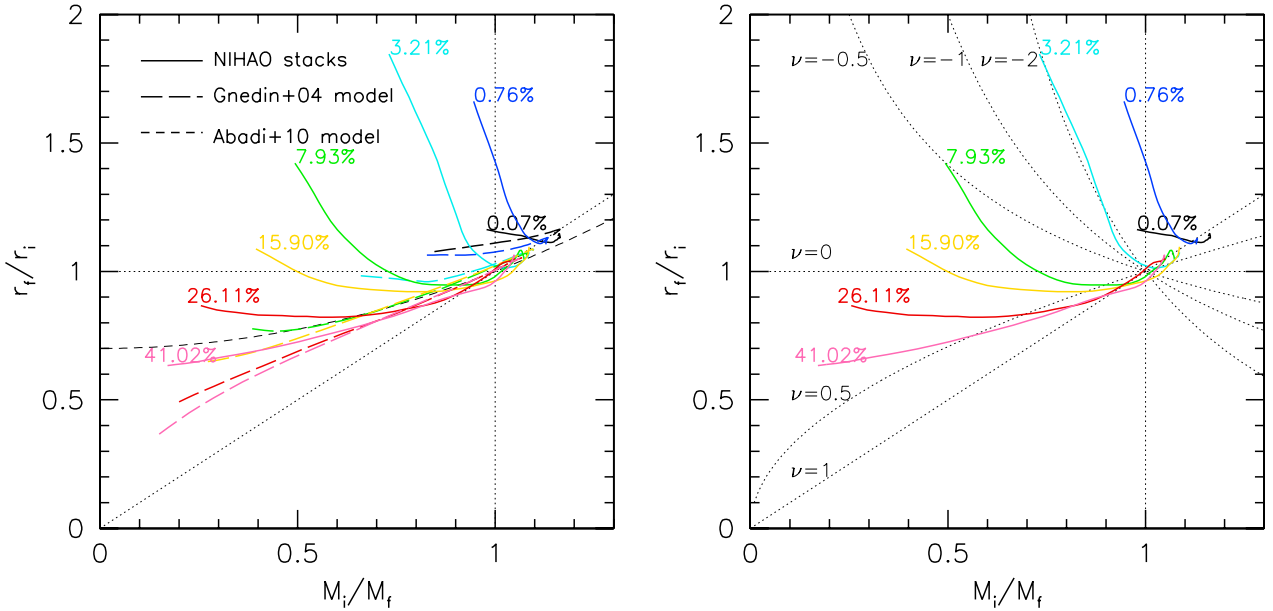


Figure 11. Comparison between halo response in NIHAO simulations (binned by star formation efficiency, solid lines), and various models in the literature. Left: long-dashed lines show the halo response predicted by the model of Gnedin et al. (2004), which is different for each NIHAO stack, while the short dashed line shows the relation from Abadi et al. (2010). Right: dotted lines show $r_f/r_i = (M_i/M_f)^\nu$ which is sometimes used to parametrize the halo response in galaxy mass models. None of these models is able to capture the full variation in halo response.

the gas removal is thus

$$E = -\frac{G(1-f_{\text{out}})^2 M^2}{r_a} + \frac{1}{2}(1-f_{\text{out}})MV_a^2, \quad (14)$$

with V_a given above. Then the shell expands while conserving energy to a new radius r_f in a new virial equilibrium (total energy = half the potential energy), so the energy is

$$E = -\frac{1}{2}\frac{G(1-f_{\text{out}})^2 M^2}{r_f}. \quad (15)$$

Equating the energies and inserting V_a we obtain

$$\frac{r_f}{r_a} = \frac{1-f_{\text{out}}}{1-2f_{\text{out}}}, \quad \frac{M_f}{M_a} = 1-f_{\text{out}}. \quad (16)$$

In the extreme case of losing half the mass, $f_{\text{out}} = 1/2$, we get $r_f \rightarrow \infty$, namely the system becomes unbound. In the limit $f_{\text{out}} \ll 1$, to first order in f_{out} , $r_f/r_a \simeq 1 + f_{\text{out}}$. So to first order in f_{out} , the effect is the same as in an adiabatic expansion, which would have been $r_f/r_a = (1-f_{\text{out}})^{-1} \simeq (1+f_{\text{out}})$. However, the higher orders in f_{out} make the impulse expansion stronger than the adiabatic case.

One can show that the expansion for one episode with a given f_{out} is larger than the expansion for two episodes with $f_{\text{out}}/2$ each. And thus the net outflow is not necessarily a robust predictor of the halo response.

4.3.3 Adiabatic contraction and impulsive expansion

Now let us assume an adiabatic inflow with mass fraction f_{in} followed by an instantaneous outflow of mass fraction f_{out} , with the inflow and outflow fractions related by

$$f_{\text{out}} = \beta f_{\text{in}}. \quad (17)$$

Combining equations (11) & (16), we obtain

$$\frac{r_f}{r_i} = \frac{(1-\beta f_{\text{in}})(1-f_{\text{in}})}{1-2\beta f_{\text{in}}}, \quad \frac{M_f}{M_i} = \frac{1-\beta f_{\text{in}}}{1-f_{\text{in}}}. \quad (18)$$

For equal inflow and outflow fractions $f_{\text{out}} = f_{\text{in}} \equiv f$ ($\beta = 1$), the result is net expansion. For net inflow ($\beta < 1$), for small values of f there is a net contraction, while for large values of f there is net expansion (See Fig. 12). The boundary occurs at $f_{\text{out}} = 1 - \beta$ and $f_{\text{in}} = \beta^{-1} - 1$. Since $0 \leq f_{\text{in}} < 1$, contraction occurs at all values of f_{in} when $\beta < 0.5$, i.e., the inflow fraction is more than double the outflow fraction.

For $f_{\text{in}} \ll 1$ we get

$$\frac{r_f}{r_i} \simeq 1 - (1-\beta)f_{\text{in}} + \beta(2\beta-1)f_{\text{in}}^2, \quad (19)$$

and thus for $\beta = 1$ the effect is second order in f_{in} .

4.3.4 Cycles of inflow and outflow

If the removed gas remains bound and falls back to the centre, or if fresh gas accretes, more than one cycle of inflow and outflow can occur (e.g., Read & Gilmore 2005). An upper limit to the number of cycles is set by the dynamical time. At the virial radius $t_{\text{dyn}} \sim 1 \text{ Gyr } h(z)^{-1}$, where $h(z) = H(z)/100 \text{ km s}^{-1} \text{ Mpc}^{-1}$, is the Hubble parameter. Thus if the gas reaches the virial radius, roughly 10 cycles are possible in a Hubble time. Since circular velocity is approximately constant inside a dark matter halo, the dynamical time is smaller at smaller radii: $t_{\text{dyn}} \sim 1 \text{ Gyr } (R/R_{200})h(z)^{-1}$. At the scale of the half-mass radius of the stars $\sim 0.01R_{200}$, the dynamical time is thus $\sim 10 \text{ Myr}$. Thus ~ 1000 cycles are in principle possible in a Hubble time.

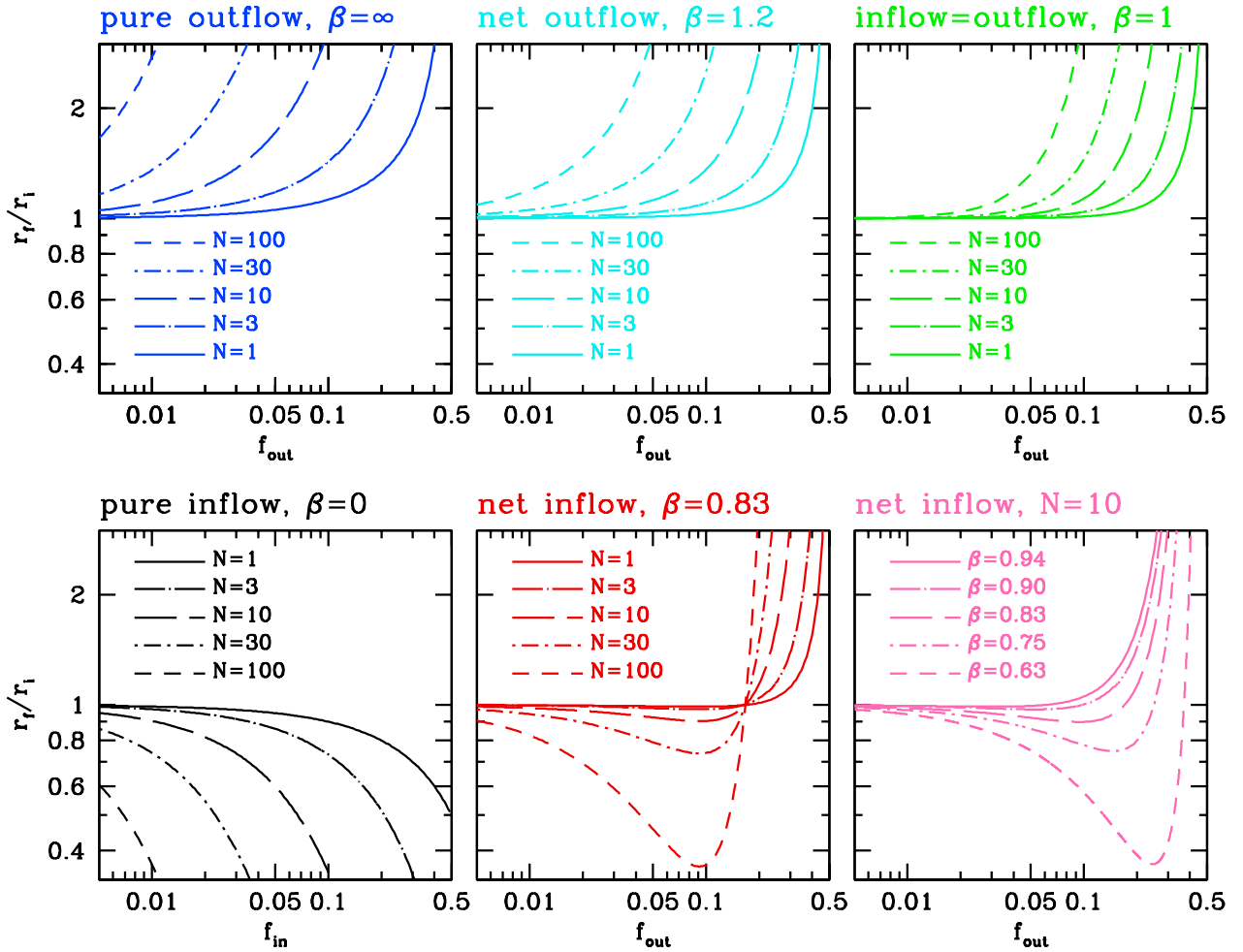


Figure 12. Toy model for adiabatic contraction and impulsive expansion. These plots show the change in radii of a shell, r_f/r_i , versus the fraction of mass in the adiabatic inflow (f_{in}) or impulsive outflow (f_{out}), with a ratio $\beta = f_{\text{out}}/f_{\text{in}}$ and N cycles. Lower left: pure inflow ($\beta = 0$) leads to contraction ($r_f/r_i < 1$). Upper left: pure outflow leads to expansion ($r_f/r_i > 1$). For a single event, $N = 1$, the halo response is only significant for $f_{\text{out}} \gtrsim 0.3$, while for multiple events even small values of f_{out} can have large cumulative effects. Upper middle: net outflow with $\beta = 1.2$ results weaker expansion than the pure inflow case. Upper right: equal inflow and outflow fractions ($\beta = 1$), repeated N times results in expansion for all values of f_{out} . Lower middle: when there is net inflow (e.g., $\beta = 0.83$) contraction occurs for $f_{\text{out}} < (1 - \beta)$ and expansion for $f_{\text{out}} > (1 - \beta)$. More cycles results in larger departures of r_f/r_i from unity. Lower right: net inflow with $N = 10$ cycles and different β can result in the same maximum contraction factors as variable N at fixed β .

Fig. 11 of Tollet et al. (2016) shows the mass fractions of stars gas and dark matter inside 2kpc as a function of time for three NIHAO haloes of mass $\sim 10^{10}, 10^{11}$, and $10^{12}M_{\odot}$. At the time resolution of the plot, we see ~ 10 cycles in a Hubble time where the gas fraction varies by ~ 0.1 .

If each cycle has a different f_{in} and f_{out} , then the net contraction factor r_f/r_i , is simply the product of the contraction factors of the separate episodes. A special case is when the same cycle is repeated N times, for which

$$\frac{r_f}{r_i} = \left[\frac{(1 - f_{\text{in}})(1 - \beta f_{\text{in}})}{(1 - 2\beta f_{\text{in}})} \right]^N, \quad \frac{M_f}{M_i} = \left[\frac{1 - \beta f_{\text{in}}}{1 - f_{\text{in}}} \right]^N. \quad (20)$$

For N large enough, the expansion (for $f_{\text{out}} > 1 - \beta$) can be as large as desired. For $\beta = 1$ (i.e., equal inflow and outflow fractions) and $f \ll 1$ it becomes

$$\frac{r_f}{r_i} \simeq 1 + Nf^2. \quad (21)$$

For small values ($f_{\text{out}} \lesssim 0.1$), inflows and outflows have almost symmetric effects, leading to no net change in the halo profile even for large N . For large values of f_{out} , the expansive effects of outflows overcomes the contractive effects of inflows. In the case of equal inflow and outflow, the net effect is expansion (upper right panel in Fig. 12). However, unless f_{out} is close to 0.5, or N is large, the net change is only small. If the net effect is inflow (lower middle panel), the halo will tend to contract for small values of f_{out} (corresponding to large radii) and expand for high values of f_{out} (corresponding to small radii). The example of $\beta = 0.83$ is shown. In this case the maximum contraction occurs for $f_{\text{out}} \sim 0.1$, while no change occurs at $f_{\text{out}} \sim 0.17$, and expansion for higher values of f_{out} .

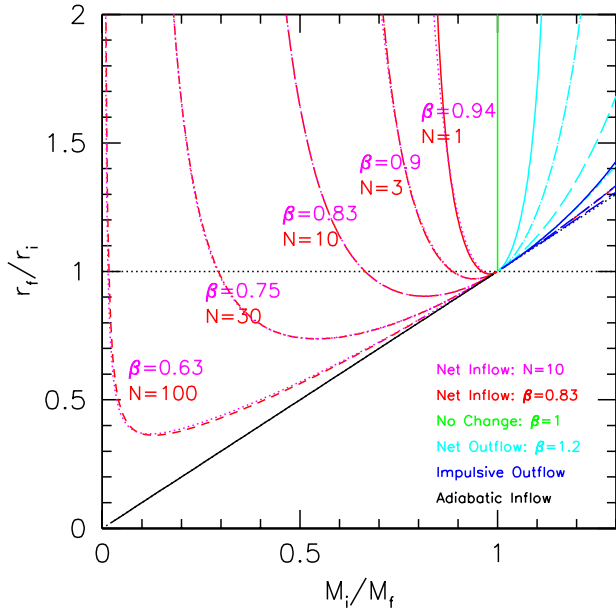


Figure 13. Results in the halo response plane for a toy model of N cycles of adiabatic inflow followed by impulsive outflow. Colour and line types are the same as in Fig. 12. Adiabatic contraction corresponds to the black diagonal line. For the case of net inflow very similar tracks can be found for different combinations of β and N . Red lines show models with $\beta = 0.83$ and N varying from 1 to 100, while magenta lines show models with $N = 10$ and β varying from 0.94 to 0.63.

4.3.5 Degeneracy between number of cycles and flow ratio

Very similar tracks in the halo response mass radius plane can be achieved with different combinations of N and β (see Fig. 13). This degeneracy can be characterized by comparing the mass ratios where there is no change in the radii: $r_f/r_i = 0$ when $f_{\text{in}} = \beta^{-1} - 1$, and $M_i/M_f = (2\beta - 1)^N / \beta^{2N}$. Thus if we wish to keep an integer number of cycles, it makes sense to express β in terms of M_i/M_f and N , thus $\beta = (1 - \sqrt{1 - (M_i/M_f)^{1/N}}) / (M_i/M_f)^{1/N}$. For example if we set $M_i/M_f = 0.5$, we get the degenerate solutions: $(N, \beta) = (1, 0.586); (10, 0.794); (100, 0.923)$. This degeneracy means we cannot uniquely infer the number of cycles and inflow to outflow fraction based on the path of simulations in the halo response plane.

4.3.6 Bathtub model

The bathtub model (Dekel & Mandelker 2014) allows us to express β for the galaxy in terms of the star formation efficiency via

$$\beta = 1 - \epsilon_{\text{SF}}/p \quad (22)$$

where p is the penetration factor: $p = \text{inflow rate on to galaxy} / \text{inflow rate into halo}$. For $\sim 10^{12} M_{\odot}$ haloes at $z \sim 2$, Dekel et al. (2013) finds $p \sim 0.5$. For simplicity here we assume $p = 1$. In future, we will calibrate this as a function of mass and redshift against our simulations. The bathtub model can also be used to link other properties of the out-

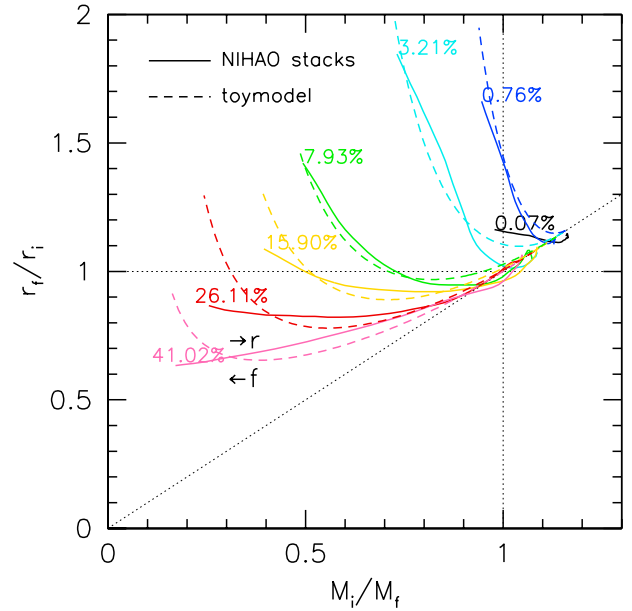


Figure 14. Average halo response for NIHAO haloes binned by star formation efficiency (solid lines) compared to the toy model (dashed lines), see the text for details. The arrows show the direction of increasing radius, r , in the simulation, and outflow fraction, f , in the toy model.

flow, such as the mass loading factor, to the halo response (see Dekel et al. , in preparation).

4.3.7 Comparison to simulations

The halo response at a given radius, is thus determined by the value of f_{out} and f_{in} at that radius and by N . Consider the simple case of the removal of an amount of gas from near the centre of the halo to beyond the virial radius. Since the mass removed is fixed, while the total mass at each radius increases, f_{out} decreases monotonically with radius. Thus, the response at different radii within the halo can be spanned by varying f_{out} from $f_{\text{out}} \ll 1$ at large radii to larger values up to $f_{\text{out}} = 1/2$ (where r_f/r_i explodes in the impulse limit).

Fig. 13 shows the models from Fig. 12 in the halo response plane. The red lines show the case of $f_{\text{in}} = 1.2f_{\text{out}}$, i.e., $\beta \simeq 0.83$, with the number of cycles varying from $N = 1$ to 100. The toy model has a similar qualitative behaviour as the simulations. We can understand why the tracks reach a minimum r_f/r_i and then increase as M_i/M_f decreases: at smaller radii (and hence smaller M_i/M_f) the local gas fraction ($M_{\text{gas}}(< r)/M_{\text{tot}}(r)$) is larger, and thus the effects of impulsive outflows are larger than the contractive effects of inflows.

Fig. 14 compares the average halo response for galaxies with a given star formation efficiency with our toy model. Here we use the bathtub model to set $\beta = 1 - \epsilon_{\text{SF}}$ and vary the number of inflow and outflow cycles to roughly match the simulations. For $\epsilon_{\text{SF}} = (0.410, 0.261, 0.159, 0.079, 0.032, 0.008)$ we find $N = (3, 10, 25, 90, 200, 1000)$. Using the bathtub model we can infer the mass-loading factors using $\eta = 0.5\beta/(1 - \beta)$, obtaining $\eta = (0.72, 1.42, 2.64, 5.83, 15.1, 62)$. Additionally, in

order to match the simulations at $M_i/M_f > 1$, we add an episode of adiabatic expansion, with $f_{\text{out}} = 0.17(1 - 2\epsilon_{\text{SF}})$, corresponding to permanent gas loss from the system.

In detail the expansive effects are too strong at small M_i/M_f (small radii). This may be due to break down in the impulse approximation for high gas fractions, or if the number of cycles, N , or the outflow-to-inflow ratio, β , varies with radius, or if f or β vary time stochastically or systematically with time.

4.3.8 Comparison to Pontzen & Governato (2012)

Pontzen & Governato (2012) present a model for the response of the dark matter halo to a fluctuating potential sourced by supernova driven gas flows. Assuming a spherical potential of the form $V(r, t) = V_0(t)r^{-1}$, their equation 6 gives the energy gain in terms of the potential change

$$\frac{\Delta E}{E_0} = -2 \left(\frac{\Delta V_0}{V_0} \right)^2 = -2f^2. \quad (23)$$

Where the last equality is for the isolated shell case we study which assumes $V_0 \propto GM/r$, thus $\Delta V/V = \Delta M/M = f$ at fixed radius.

We derive a similar result in the context of our model under similar assumptions. By comparing the energy derived from the virial theorem before and after the episode of adiabatic inflow and impulsive outflow gives: $E_f = E_i(r_i/r_f)$, and thus the change in energy is $\Delta E = E_i(r_i/r_f - 1)$. Assuming small f and $\beta = 1$ gives $\Delta E/E_i = -f^2$. Re-deriving the equation for impulsive inflows and outflows, we find $\Delta E/E_i = -2f^2$, in agreement with equation (23). The overall effect when using impulsive inflows is larger because they have less of a contractive effect than adiabatic inflows.

5 DISCUSSION

We now discuss the various phases of halo response and how they are related to physical properties of the galaxies. We then compare our results with those found in the literature.

5.1 Inflow versus outflow

The upper panels of Fig. 15 show ratio between baryonic mass inside $0.01R_{200}$ in the hydro and DMO simulations versus stellar mass fraction within $0.01R_{200}$ (upper left) and change in dark matter masses within $0.01R_{200}$ (upper right). Points are colour coded by change in dark matter mass. No change is yellow, black is the most expansion and magenta is the most contraction. The upper-right panel is divided into four quadrants. Lower right is unphysical (contracted dark matter with expanded baryons) and reassuringly all simulations avoid this region. Lower left is expansion in both dark matter and baryons. The upper left is when the dark matter expands but there is net inflow of baryons, with greater inflow resulting in less expansion. The trend continues to the upper right where more inflow leads to more contraction of the dark matter. Contraction starts when the baryonic mass increases by a factor of ~ 10 . At this point, the baryons start to dominate the total mass budget at small radii.

The upper-left panel shows that at low ϵ_{SF} there is no net change in baryon content. For intermediate $\epsilon_{\text{SF}} \sim 0.01$,

there is actually less baryons inside $0.01R_{200}$ than if the baryons trace the DMO simulation. Thus, a significant fraction of the baryons that cooled have been ejected. Perhaps, not surprisingly, these galaxies have the strongest expansion. Above $\epsilon_{\text{SF}} = 0.03$ we see net inflow of baryons, and the stars start to dominate the baryon budget so there is a tight correlation between the axes.

5.2 The role of gas

Gas plays an important role in two ways: (1) gas accretion drives contraction; and (2) gas outflows cause significant expansion only if the gas fraction is high enough to allow $f_{\text{out}} \gtrsim 0.1$ (see Fig.12). The lower panels of Fig. 15 shows the gas fraction versus stellar mass fraction (left) and the dark matter mass ratio (right). All quantities are measured at 1% of the virial radius. Points are colour coded by the dark matter mass ratio. Since the gas fraction can fluctuate wildly on small time-scales due to SN feedback (e.g., Tollet et al. 2016), we focus on the average gas fractions, which correlate with both star formation efficiency and the halo response. We verified that the galaxies with halo expansion and low gas fractions inside of $0.01R_{200}$ are in fact gas rich, with global cold gas to stellar mass ratios in excess of 1. Contraction only occurs when the gas fraction is low ($\lesssim 0.1$), while the most expansion occurs when the gas fraction is high ~ 0.3 . These trends are consistent with the expectation of our toy model.

5.3 The role of star formation

Star formation play two roles: (1) star formation drives expansion from the high mass stars that turn into supernovae. (2) However, since stars are collisionless, once formed they behave the same way as the dark matter and are effectively added to the overall potential. Subsequent star formation episodes will face a deeper potential, and find it harder to escape. If there is no new supply of gas, the reduction of gas will also weaken the expansive effects of any outflows.

5.4 Comparison to previous results

Several authors have studied the halo response in cosmological galaxy formation simulations finding contraction in haloes of mass $\sim 10^{12}M_{\odot}$ (Gnedin et al. 2004; Abadi et al. 2010; Pedrosa et al. 2010). It should be noted that these studies suffered from over-cooling and small sample sizes (the Abadi et al. 2010 simulations do not include star formation). So it is not clear how relevant they are to typical galaxies. Nevertheless, in our simulations, when the star formation efficiency is high we also find haloes contract strongly, in broad agreement with these earlier studies.

Di Cintio et al. (2014a), used the MaGICC simulations (Stinson et al. 2013) to study the dark matter density slopes in the inner 1-2 per cent of the virial radius. They found a non-linear dependence between the inner slope and stellar to halo mass. This result has been confirmed with a larger sample of galaxies from NIHAO (Tollet et al. 2016), and a small sample of higher resolution galaxies from FIRE (Chan et al. 2015). Since we use the same simulations our results are consistent with Di Cintio et al. (2014a) and Tollet et al. (2016).

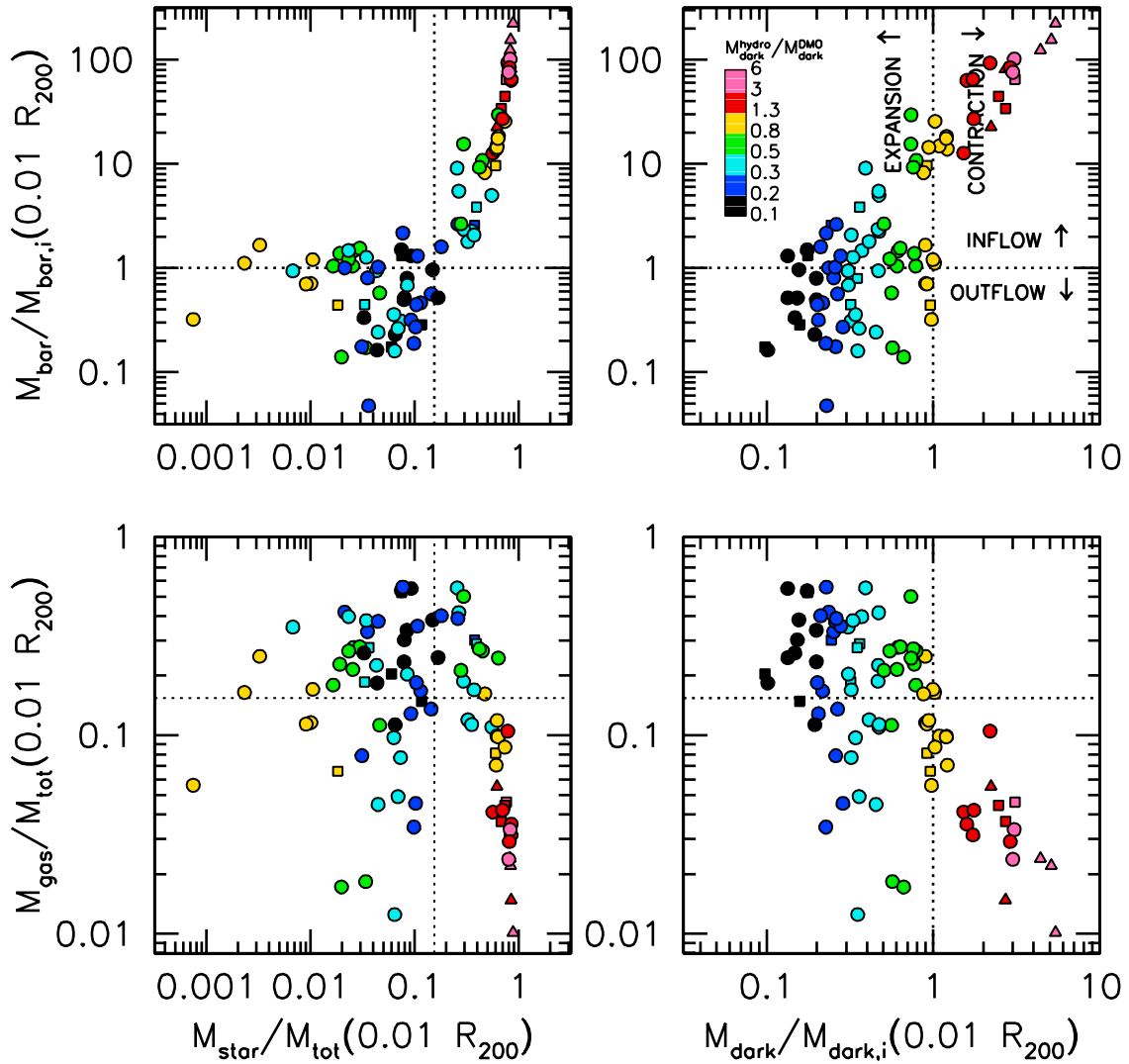


Figure 15. Correlations between halo response, star formation efficiency, gas fraction, and baryonic mass ratio, all measured at 1% of the virial radius. Points are colour coded by the halo response. Dotted lines correspond to either unity or the cosmic baryon fraction ($f_{\text{bar}} = 0.154$).

Going a step further, Di Cintio et al. (2014b, DC14) present a dark matter density profile dependent on ϵ_{SF} based on 10 simulations with the fiducial MaGICC feedback. As discussed in §3.5, the DC14 model likely overestimates the expansion at $\epsilon_{\text{SF}} \sim 0.01$ and overestimates the contraction at $\epsilon_{\text{SF}} \gtrsim 0.2$, although the qualitative dependence of halo contraction and expansion on ϵ_{SF} remains the same.

The EAGLE project (Schaye et al. 2015) has formed galaxies with reasonable star formation efficiencies and galaxy sizes over a wide range of masses. When looking at average halo profiles in bins of halo mass from $M_{200} = 10^{10}$ to $10^{14} M_{\odot}$, Schaller et al. (2015) finds almost no difference in dark matter profiles between hydro and DMO simulations. As touched on in § 3.2, an important issue is resolution. For haloes of mass $M_{200} \sim 10^{11} M_{\odot}$ (the scale where we find the most expansion in our simulations), their convergence radius is 5% of the virial radius. Looking at Fig. 3 we

find very little expansion (or contraction) above this scale, and thus their lack of expansion is expected. At the MW mass scale ($M_{200} \sim 10^{12} M_{\odot}$), their simulations find very little change in the halo mass profile, as we do. So our respective simulations may actually be more consistent than at first apparent.

Another potential source of differences in halo response is the threshold for star formation. NIHAO and MaGICC uses $n_{\text{th}} \simeq 10$ while EAGLE adopts a much lower threshold of $n_{\text{th}} \lesssim 0.1$. A lower threshold is expected to result in a more uniform star formation history, with fewer starbursts, and hence fewer outflow events with high f_{out} , and thus weaker expansion. However, Dutton et al. (2015) found halo expansion that follows the NIHAO results in the progenitors of massive elliptical galaxies using a threshold of $n_{\text{th}} \sim 1 \text{ cm}^{-3}$, and the FIRE simulations (Chan et al. 2015) are also consistent with NIHAO (from dwarfs to MW mass haloes)

and use a higher threshold of $n_{\text{th}} > 10 - 100 \text{ cm}^{-3}$. Thus the halo response does not seem strongly sensitive to the star formation threshold, at least for $n_{\text{th}} > 1 \text{ cm}^{-3}$. Determining how sensitive the halo response is to the sub-grid model for star formation and feedback needs to be studied in greater detail.

6 SUMMARY

We use ~ 100 hydrodynamical cosmological zoom-in simulations from NIHAO, MaGICC, and MUGS (Wang et al. 2015; Stinson et al. 2013, 2010) to investigate the response of CDM haloes to baryonic galaxy formation processes. We define the halo response as the change in dark matter mass profiles, at a given radius, between hydrodynamical and dissipationless simulations. We summarize our results as follows:

- There is a much wider diversity of dark matter halo profiles in hydrodynamical simulations than dissipationless simulations (Fig. 2). The halo response to galaxy formation thus breaks the scale free nature of CDM haloes.

- Dark matter haloes are only significantly modified at radii below $\sim 0.05R_{200}$ (Fig. 3), and thus sufficiently high resolution is required to see the effects.

- The halo response is correlated with halo mass, M_{200} , stellar mass, M_{star} , integrated star formation efficiency, $\epsilon_{\text{SF}} = (M_{\text{star}}/M_{200})/(\Omega_{\text{b}}/\Omega_{\text{m}})$, and the compactness of the galaxy, $\epsilon_{\text{R}} = r_{1/2}/R_{200}$. The correlation with ϵ_{SF} has the smallest scatter (0.15 dex), while the correlation with galaxy compactness is well described with a power-law above $\epsilon_{\text{SF}} \sim 10^{-3}$ (Fig. 4).

- The halo response at any radius is proportional to $\epsilon_{\text{R}}/\epsilon_{\text{SF}}^{0.13}$, with a shallower slope at larger radii (Fig. 6). We provide an empirical formula (Fig. 7), section 3.4, that reproduces the response of the dark matter haloes on scales from $0.01R_{200}$ to R_{200} (Fig. 8).

- The path of galaxies in the $r_{\text{f}}/r_{\text{i}}$ versus $M_{\text{i}}/M_{\text{f}}$ plane of the adiabatic contraction formalism depends on ϵ_{SF} (Fig. 10). Galaxies with high star formation efficiencies ($\epsilon_{\text{SF}} \gtrsim 0.5$) have contraction close to that of the adiabatic contraction formalism of Gnedin et al. (2004). For lower ϵ_{SF} the contraction is progressively weaker, first leading to expansion at small $M_{\text{i}}/M_{\text{f}}$, and then at all $M_{\text{i}}/M_{\text{f}}$. Finally when ϵ_{SF} is very low, the halo response is weak.

- The paths of galaxies in the $r_{\text{f}}/r_{\text{i}}$ versus $M_{\text{i}}/M_{\text{f}}$ plane can be understood by a toy model consisting of several cycles of adiabatic inflows followed by impulsive outflows (Fig. 14). Pure inflows result in contraction, while pure outflows result in expansion. For equal inflow and outflow fractions, f , the net effect is expansion. For net inflow, contraction occurs for small f (i.e., large radii), while expansion occurs for large f (i.e., small radii).

- For significant halo expansion to occur the local gas fraction needs to be $\gtrsim 0.1$ (Fig. 15). Even if there is sufficient energy to drive an outflow, if there is not enough gas, the expansive effects of the outflow will be minimal.

Our results on the halo response to galaxy formation can be coupled to results from dissipationless simulations to make predictions for the structure of CDM haloes. Since our model for star formation and feedback is by no means

unique, at present it is not clear whether our fitting formula for the halo response is applicable to other subgrid models. Thus, our predictions are not yet at the stage that they can be used to falsify the CDM model. Nevertheless, the regularities present in our simulations suggest that, despite the many complex processes involved in galaxy formation, a fully predictive model for the structure of CDM haloes may soon be possible.

Determining on which mass and radial scales different subgrid models agree / disagree on the halo response is an important subject for future studies. Also it would be interesting to find additional observable/modelable parameters, besides ϵ_{SF} and ϵ_{R} , that the halo response correlates with.

ACKNOWLEDGEMENTS

This research was carried out on the High Performance Computing resources at New York University Abu Dhabi; on the THEO cluster of the Max-Planck-Institut für Astronomie and the HYDRA cluster at the Rechenzentrum in Garching; and the MW supercomputer, which is funded by the Deutsche Forschungsgemeinschaft (DFG) through Collaborative Research Center (SFB 881) ‘The Milky Way System’ (subproject Z2) and hosted and co-funded by the Jülich Supercomputing Center (JSC). We greatly appreciate the contributions of all these computing allocations. This work was supported by Sonderforschungsbereich SFB 881 ‘The Milky Way System’ (subprojects A1 and A2) of the German Research Foundation (DFG). The analysis made use of the PYNBODY package (Pontzen et al. 2013). AD acknowledges support by ISF grant 24/12, by the I-CORE Program of the PBC - ISF grant 1829/12, by BSF grant 2014-273, and by NSF grants AST-1010033 and AST-1405962. XK acknowledge the support from NSFC project no.11333008 and the ‘Strategic Priority Research Program the Emergence of Cosmological Structures’ of the CAS(No.XD09010000).

REFERENCES

- Abadi, M. G., Navarro, J. F., Fardal, M., Babul, A., & Steinmetz, M. 2010, MNRAS, 407, 847
- Baldry, I. K., Driver, S. P., Loveday, J., et al. 2012, MNRAS, 421, 621
- Behroozi, P. S., Wechsler, R. H., & Conroy, C. 2013, ApJ, 770, 57
- Blumenthal, G. R., Faber, S. M., Flores, R., & Primack, J. R., 1986, ApJ, 301, 27
- Bovy, J., & Rix, H.-W. 2013, ApJ, 779, 115
- Brook, C. B., Governato, F., Roškar, R., et al. 2011, MNRAS, 415, 1051
- Brook, C. B., Stinson, G., Gibson, B. K., Wadsley, J., & Quinn, T. 2012, MNRAS, 424, 1275
- Brook, C. B., Santos-Santos, I., & Stinson, G. 2016, MNRAS, 459, 638
- Brooks, A., & Christensen, C. 2016, Galactic Bulges, 418, 317
- Bullock, J. S., Kolatt, T. S., Sigad, Y., Somerville, R. S., Kravtsov, A. V., Klypin, A. A., Primack, J. R., & Dekel, A. 2001, MNRAS, 321, 559
- Butsky, I., Macciò, A. V., Dutton, A. A., et al. 2015, arXiv:1503.04814
- Chabrier, G. 2003, PASP, 115, 763
- Chan, T. K., Kereš, D., Oñorbe, J., et al. 2015, MNRAS, 454, 2981

- Cole, D. R., Dehnen, W., & Wilkinson, M. I. 2011, *MNRAS*, 416, 1118
- Conroy, C., & Wechsler, R. H. 2009, *ApJ*, 696, 620
- Courteau, S., & Dutton, A. A. 2015, *ApJL*, 801, L20
- Crain, R. A., Schaye, J., Bower, R. G., et al. 2015, *MNRAS*, 450, 1937
- Croton, D. J., Springel, V., White, S. D. M., et al. 2006, *MNRAS*, 365, 11
- de Blok, W. J. G., McGaugh, S. S., Bosma, A., & Rubin, V. C. 2001, *ApJL*, 552, L23
- Dekel, A., & Silk, J. 1986, *ApJ*, 303, 39
- Dekel, A., Devor, J., & Hetzroni, G. 2003, *MNRAS*, 341, 326
- Dekel, A., Zolotov, A., Tweed, D., et al. 2013, *MNRAS*, 435, 999
- Dekel, A., & Mandelker, N. 2014, *MNRAS*, 444, 2071
- Diemer, B., & Kravtsov, A. V. 2015, *ApJ*, 799, 108
- Di Cintio, A., Brook, C. B., Macciò, A. V., et al. 2014a, *MNRAS*, 437, 415
- Di Cintio, A., Brook, C. B., Dutton, A. A., Macciò, A. V., Stinson, G. S., Knebe, A. 2014b, *MNRAS*, 441, 2986
- Duffy, A. R., Schaye, J., Kay, S. T., Dalla Vecchia, C., Battye, R. A., & Booth, C. M. 2010, *MNRAS*, 405, 2161
- Dutton, A. A., van den Bosch, F. C., Dekel, A., & Courteau, S. 2007, *ApJ*, 654, 27
- Dutton, A. A. 2009, *MNRAS*, 396, 121
- Dutton, A. A., Treu, T., Brewer, B. J., et al. 2013, *MNRAS*, 428, 3183
- Dutton, A. A., Macciò, A. V., Mendel, J. T., & Simard, L. 2013, *MNRAS*, 432, 2496
- Dutton, A. A., & Treu, T. 2014, *MNRAS*, 438, 3594
- Dutton, A. A., & Macciò, A. V. 2014, *MNRAS*, 441, 3359
- Dutton, A. A., Macciò, A. V., Stinson, G. S., et al. 2015, *MNRAS*, 453, 2447
- Dutton, A. A., Macciò, A. V., Frings, J., et al. 2016, *MNRAS*, 457, L74
- Einasto, J. 1965, *Trudy Astrofizicheskogo Instituta Alma-Ata*, 5, 87
- El-Zant, A., Shlosman, I., & Hoffman, Y. 2001, *ApJ*, 560, 636
- El-Zant, A., Freundlich, J., & Combes, F. 2016, *arXiv:1603.00526*
- Garrison-Kimmel, S., Bullock, J. S., Boylan-Kolchin, M., & Bardwell, E. 2016, *arXiv:1603.04855*
- Gill, S. P. D., Knebe, A., & Gibson, B. K. 2004, *MNRAS*, 351, 399
- Gnedin, O. Y., Kravtsov, A. V., Klypin, A. A., & Nagai, D. 2004, *ApJ*, 616, 16
- Goeddt, T., Moore, B., Read, J. I., Stadel, J., & Zemp, M. 2006, *MNRAS*, 368, 1073
- Governato, F., Zolotov, A., Pontzen, A., et al. 2012, *MNRAS*, 422, 1231
- Gustafsson, M., Fairbairn, M., & Sommer-Larsen, J. 2006, *Phys-RevD*, 74, 123522
- Gutcke, T. A., Stinson, G. S., Macciò, A. V., Wang, L., & Dutton, A. A. 2016, *arXiv:1602.06956*
- Hammer, F., Puech, M., Chemin, L., Flores, H., & Lehnert, M. D. 2007, *ApJ*, 662, 322
- Hopkins, P. F., Kereš, D., Oñorbe, J., et al. 2014, *MNRAS*, 445, 581
- Hudson, M. J., Gillis, B. R., Coupon, J., et al. 2015, *MNRAS*, 447, 298
- Jardel, J. R., & Sellwood, J. A. 2009, *ApJ*, 691, 1300
- Johansson, P. H., Naab, T., & Ostriker, J. P. 2009, *ApJL*, 697, L38
- Keller, B. W., Wadsley, J., Benincasa, S. M., & Couchman, H. M. P. 2014, *MNRAS*, 442, 3013
- Klypin, A. A., Trujillo-Gomez, S., & Primack, J. 2011, *ApJ*, 740, 102
- Knollmann, S. R., & Knebe, A. 2009, *ApJS*, 182, 608
- Kravtsov, A. V. 2013, *ApJL*, 764, L31
- Kroupa, P., Tout, C. A., & Gilmore, G. 1993, *MNRAS*, 262, 545
- Leauthaud, A., Tinker, J., Bundy, K., et al. 2012, *ApJ*, 744, 159
- Ludlow, A. D., Bose, S., Angulo, R. E., et al. 2016, *MNRAS*, 460, 1214
- Macciò, A. V., Dutton, A. A., & van den Bosch, F. C. 2008, *MNRAS*, 391, 1940
- Macciò, A. V., Stinson, G., Brook, C. B., et al. 2012, *ApJL*, 744, L9
- Macciò, A. V., Mainini, R., Penzo, C., & Bonometto, S. A. 2015, *MNRAS*, 453, 1371
- Maller, A. H., & Dekel, A. 2002, *MNRAS*, 335, 487
- Marinacci, F., Pakmor, R., & Springel, V. 2014, *MNRAS*, 437, 1750
- Martizzi, D., Teyssier, R., Moore, B., & Wentz, T. 2012, *MNRAS*, 422, 3081
- Martizzi, D., Teyssier, R., & Moore, B. 2013, *MNRAS*, 432, 1947
- Mashchenko, S., Couchman, H. M. P., & Wadsley, J. 2006, *Natur*, 442, 539
- Mashchenko, S., Wadsley, J., & Couchman, H. M. P. 2008, *Science*, 319, 174
- Moster, B. P., Somerville, R. S., Maulbetsch, C., et al. 2010, *ApJ*, 710, 903
- More, S., van den Bosch, F. C., Cacciato, M., Skibba, R., Mo, H. J., & Yang, X. 2011, *MNRAS*, 410, 210
- Navarro, J. F., Eke, V. R., & Frenk, C. S. 1996, *MNRAS*, 283, L72
- Navarro, J. F., Frenk, C. S., & White, S. D. M. 1997, *ApJ*, 490, 493 (NFW)
- Navarro, J. F., et al. 2010, *MNRAS*, 402, 21
- Newman, A. B., Treu, T., Ellis, R. S., & Sand, D. J. 2013, *ApJ*, 765, 25
- Obreja, A., Brook, C. B., Stinson, G., et al. 2014, *MNRAS*, 442, 1794
- Obreja, A., Stinson, G. S., Dutton, A. A., et al. 2016, *MNRAS*, 459, 467
- Oh, S.-H., de Blok, W. J. G., Brinks, E., Walter, F., & Kennicutt, R. C., Jr. 2011, *AJ*, 141, 193
- Pagels, H., & Primack, J. R. 1982, *Physical Review Letters*, 48, 223
- Pedrosa, S., Tissera, P. B., & Scannapieco, C. 2010, *MNRAS*, 402, 776
- Peñarrubia, J., Gómez, F. A., Besla, G., Erkal, D., & Ma, Y.-Z. 2016, *MNRAS*, 456, L54
- Planck Collaboration, Ade, P. A. R., Aghanim, N., et al. 2014, *A&A*, 571, A16
- Pontzen, A., & Governato, F. 2012, *MNRAS*, 421, 3464
- Pontzen, A., Roškar, R., Stinson, G., & Woods, R. 2013, *Astrophysics Source Code Library*, 1305.002
- Power, C., Navarro, J. F., Jenkins, A., et al. 2003, *MNRAS*, 338, 14
- Read, J. I., & Gilmore, G. 2005, *MNRAS*, 356, 107
- Reddick, R. M., Wechsler, R. H., Tinker, J. L., & Behroozi, P. S. 2013, *ApJ*, 771, 30
- Romano-Díaz, E., Shlosman, I., Hoffman, Y., & Heller, C. 2008, *ApJL*, 685, L105
- Sawala, T., Frenk, C. S., Fattahi, A., et al. 2016, *MNRAS*, 457, 1931
- Schaller, M., Frenk, C. S., Bower, R. G., et al. 2015, *MNRAS*, 451, 1247
- Schaye, J., Crain, R. A., Bower, R. G., et al. 2015, *MNRAS*, 446, 521
- Sellwood, J. A. 2008, *ApJ*, 679, 379
- Shen, S., Wadsley, J., & Stinson, G. 2010, *MNRAS*, 407, 1581
- Somerville, R. S., Hopkins, P. F., Cox, T. J., Robertson, B. E., & Hernquist, L. 2008, *MNRAS*, 391, 481
- Sonnenfeld, A., Treu, T., Marshall, P. J., et al. 2015, *ApJ*, 800, 94
- Spergel, D. N., & Steinhardt, P. J. 2000, *Physical Review Letters*, 84, 3760

- Spergel, D. N., Bean, R., Doré, O., et al. 2007, *ApJS*, 170, 377
- Stadel, J., Potter, D., Moore, B., et al. 2009, *MNRAS*, 398, L21
- Stinson, G., Seth, A., Katz, N., et al. 2006, *MNRAS*, 373, 1074
- Stinson, G. S., Bailin, J., Couchman, H., et al. 2010, *MNRAS*, 408, 812
- Stinson, G. S., Brook, C., Macciò, A. V., et al. 2013, *MNRAS*, 428, 129
- Stinson, G. S., Dutton, A. A., Wang, L., et al. 2015, *MNRAS*, 454, 1105
- Swaters, R. A., Madore, B. F., van den Bosch, F. C., & Balcells, M. 2003, *ApJ*, 583, 732
- Tissera, P. B., White, S. D. M., Pedrosa, S., & Scannapieco, C. 2010, *MNRAS*, 406, 922
- Tollet, E., Macciò, A. V., Dutton, A. A., et al. 2016, *MNRAS*, 456, 3542
- Trujillo-Gomez, S., Klypin, A., Colín, P., et al. 2015, *MNRAS*, 446, 1140
- Vogelsberger, M., Genel, S., Springel, V., et al. 2014, *MNRAS*, 444, 1518
- Wadsley, J. W., Stadel, J., & Quinn, T. 2004, *NewA*, 9, 137
- Walker, M. G., & Peñarrubia, J. 2011, *ApJ*, 742, 20
- Wang, L., Dutton, A. A., Stinson, G. S., Macciò, A. V., Penzo, C., Kang, X., Keller, B. W., Wadsley, J. 2015, *MNRAS*, 454, 83
- Wang, L., Dutton, A. A., Stinson, G. S., et al. 2016, *arXiv:1601.00967*
- Weinberg, M. D., & Katz, N. 2002, *ApJ*, 580, 627
- Zhao, D. H., Jing, Y. P., Mo, H. J., Börner, G. 2009, *ApJ*, 707, 354